Peer reviewed paper

Title: Hydromechanical characterization of CO_2 injection sites

Authors: Víctor Vilarrasa, Jesús Carrera and Sebastià Olivella

Journal published: International Journal of Greenhouse Gas Control

Volume and pages: doi:10.1016/j.ijggc.2012.11.014

Publication year: 2013

HYDROMECHANICAL CHARACTERIZATION OF CO_2 INJECTION SITES

Víctor Vilarrasa[1,2], Jesús Carrera[1] and Sebastià Olivella[2]

[1] GHS, Institute of Environmental Assessment and Water Research (IDAEA), CSIC, Jordi Girona 18-26, 08034 Barcelona, Spain

[2] Dept Geotechnical Engineering and Geosciences, Technical University of Catalonia (UPC-BarcelonaTech), Jordi Girona 1-3, 08034 Barcelona, Spain

ABSTRACT

Clear understanding of coupled hydromechanical effects, such as ground deformation, induced microseismicity and fault reactivation, will be crucial to convince the public that geologic carbon storage is secure. These effects depend on hydromechanical properties, which are usually determined at metric scale. However, their value at the field scale may differ in orders of magnitude. To address this shortcoming, we propose a hydromechanical characterization test to estimate the hydromechanical properties of the aquifer and caprock at the field scale. We propose injecting water at high pressure and, possibly, low temperature while monitoring fluid pressure and rock deformation. Here, we analyze the problem and perform numerical simulations and a dimensional analysis of the hydromechanical equations to obtain curves for overpressure and vertical displacement as a function of the volumetric strain term. We find that these curves do not depend much on the Poisson ratio, except for the dimensionless vertical displacement at the top of the caprock, which does. We can then estimate the values of the Young's modulus and the Poisson ratio of the aquifer and the caprock by introducing field measurements in these plots. Hydraulic parameters can be determined from the interpretation of fluid pressure evolution in the aquifer. Reverse-water level fluctuations are observed, i.e. fluid pressure drops in the caprock as a result of the induced deformation that undergoes the aquifer-caprock system when injecting in the aquifer. We find that induced microseismicity is more likely to occur in the aquifer than in the caprock and depends little on their stiffness. Monitoring microseismicity is a useful tool to track the opening of fractures. The propagation pattern depends on the stress regime, i.e. normal, strike slip or reverse faulting. The onset of microseismicity in the caprock can be used to define the maximum sustainable injection pressure to ensure a permanent CO_2 storage.

Keywords: Dimensional analysis, Noordbergum effect, induced microseismicity, stress regime, fault reactivation.

1. INTRODUCTION

Coupled hydromechanical effects, such as ground deformation, induced microseismicity and fault reactivation, should be understood and quantified to demonstrate to the public that geologic carbon storage is safe. The most representative examples of coupled hydromechanical effects may be ground heave and microseismic activity. A ground heave of 5 mm/yr has been measured on top of the carbon dioxide (CO_2) injection wells at the In Salah storage project in Algeria (Rutqvist *et al*., 2010; Vasco *et al*., 2010). Induced microseismic events were detected at Otsego County, Michigan Basin, US, due to CO_2 leakage around wells (Bohnhoff *et al*., 2010) and at the beginning of injection in the Weyburn field, Saskatchewan, Canada (Verdon *et al*., 2011). Numerically, Mazzoldi *et al*. (2012) calculated that the maximum magnitude of induced seismicity triggered in faults smaller than 1 km in length ranges from 2 to 3.9, which could be felt by the local population. This magnitude depends on the initial rock stress tensor, the length of the rupture zone and the hydromechanical properties of the fault. For instance, Cappa and Rutqvist (2012) estimated through numerical simulations that CO_2 injection in a deep aquifer bounded by a low-permeability fault can trigger earthquakes with magnitude 3, but Cappa and Rutqvist (2011b) estimated that for a similar geological setting, but in a deeper aquifer, the magnitude can be enhanced up to 4.5. Additionally, a natural high pressure CO_2 source is believed to have driven, after the occurrence of two earthquakes, thousands of aftershocks in the Northern Apennines, Italy, during more than 30 days, including four events with magnitudes ranging from 5 to 6 (Miller *et al*., 2004). Thus,

hydromechanical processes need to be well understood to define the conditions that ensure stable permanent CO_2 storage in deep geological formations.

Hydromechanical studies have focused on several aspects, including the estimation of maximum sustainable injection pressure (Streit and Hillis, 2004; Rutqvist *et al*., 2007), evaluating fault reactivation due to production of gas/oil fields (Ferronato *et al*., 2008; Soltanzadeh and Hawkes, 2009) and to CO_2 injection (Ferronato *et al*., 2010; Cappa and Rutqvist, 2011a). Fault reactivation occurs once the fault yields, which triggers microsesimicity. This microseismicity is usually due to shear-slip and produces changes in the fault aperture in the order of microns (Guglielmi *et al*. 2008). Thus, fracture permeability is enhanced, especially in the direction perpendicular to shear (Barton *et al*., 1985; Yeo *et al*., 1998; Mallikamas and Rajaram, 2005). Phillips *et al*. (2002) present three examples of induced microseismicity in sedimentary basins in which the events concentrate on the contact between layers of different mechanical properties or stress states. The evolution of the yielding region depends on the stress tensor and may propagate upwards when vertical stress is greater than horizontal stresses (Rutqvist *et al*., 2008; Vilarrasa *et al*., 2011b). To quantify these coupled hydromechanical effects, the mechanical properties of the rocks should be measured.

Mechanical properties of rocks are usually inferred from core samples at the laboratory. However, these values might not be representative at the field scale because of the existence of joints or fractures. This is illustrated by the difference between the values of the Young's modulus obtained from laboratory tests and from back-analysis of convergence measurements in underground excavations. Its value from laboratory tests is always higher than that resulting from back-analysis because fractures are more deformable than the rock matrix (e.g. Ledesma *et al*, 1996; Zhang *et al*., 2006; Cai *et*

al., 2007; Vardakos *et al*., 2007). The large-scale geomechanical properties are difficult to quantify. They can be derived from model calibration of field measurements of strain or displacements, but this requires extensive modeling work (Rutquist, 2012). Moreover, sizeable measurements usually become available a few months after the beginning of injection. A defined methodology to obtain these properties prior to injection does not exist. Therefore, it is necessary to develop a field test to characterize the macroscopic mechanical properties of the rock layers involved in CO_2 storage in deep geological formations, i.e. the reservoir and the caprock.

Pilot projects are an excellent opportunity to design and perform new tests that will be useful for CO_2 injection at the industrial scale. However, little hydromechanical field data is available in pilot projects (Kikuta *et al*., 2005; Michael *et al*., 2010) and the related studies are mainly conceptual (Chiaramonte *et al*., 2008; Smith *et al*., 2009; Vidal-Gilbert *et al*., 2010). In this context, new injection and characterization technologies are planned at the pilot site of Hontomín (Carrera *et al*., 2011), Spain. Hontomín is the injection site of the CO_2 storage Technology Demonstration Plant (TDP) of the Compostilla OXYCFB300 project, operated by Energy City Foundation (CIUDEN). Among the experiments planned for site characterization and injection technology development, a hydromechanical characterization test will be performed there. The objective of this paper is to propose a hydromechanical characterization test to obtain the macroscopic hydraulic and mechanical properties of the reservoir and the caprock and to evaluate the maximum sustainable injection pressure.

2. MECHANICAL PROPERTIES OF ROCKS

Sedimentary rocks (sandstone, limestone and dolomite) are potential host rocks for CO_2 storage. Low-permeability, high-entry pressure formations, such as shale, marl and claystone, can form the caprock. Mechanical properties of these rock types can take a wide range of values (Figures 1 and 2).

The variability of rock properties depends on the rock type. For example, reported Young's moduli of sandstones and limestones range only from 1 to 20 GPa (Goodman, 1989; Abousleiman *et al*., 2010; Heap *et al*., 2010; Hu *et al*., 2010; Rimmele *et al*., 2010). Instead, reported Young's moduli of shales range over two orders of magnitude. Soft shales, like the Boom Clay, display Young's moduli in the order of 0.1-0.4 GPa (Giraud and Rousset, 1996; Mertens *et al*., 2004; Dehandschutter *et al*., 2005; François *et al*., 2009). Stiff clays, like one from Puerto Rico, have got Young's moduli in the order of 20-40 GPa (Shalabi *et al*., 2007). Other shales (Ortega *et al*., 2010), such as oil shales (Eseme *et al*., 2007), Opalinus Clay (Thury, 2002; Gens *et al*., 2007) and Callovo-Oxfordian argillite (Zhang and Rothfuchs, 2004; Saurot *et al*., 2007; Wileveau and Bernier, 2008), have intermediate Young's modulus values, ranging from 1 to 20 GPa. The actual value of the Young's modulus increases with the mean effective stress (Dodds *et al*., 2007; Shalabi *et al*., 2007; Hu *et al*., 2010).

Poisson ratios range from 0.15 to 0.25 for the vast majority of rock samples (Figure 1). Some values close to 0.5 (incompressible) are reported in low-permeability rocks. However, these values reflect undrained conditions and are not representative of the real Poisson ratio of the rock.

The friction angle of existing fractures is important because it controls the occurrence of microseismic events. Sedimentary formations, which are formed after depositional sequences, present a high anisotropy in the directions parallel and perpendicular to bedding (Thury, 2002; Gens *et al*., 2007; Saurot *et al*., 2007). Friction angles as low as 5° (Figure 2) have been found in the direction parallel to bedding in clay-rich materials (Gens et al., 2007) or when the rock has been weakened due to demineralization (Abousleiman *et al*., 2010). Related to this, the percentage of carbonate in the clay-size material of marls affects the residual friction angle. Low carbonate content (<11%) yields residual friction angles around 12°. High carbonate content (>30%) yields residual friction angles around 30° (Frydman *et al*., 2007).

Mechanical properties of sedimentary rocks are not only highly variable, but also difficult to estimate at the field scale of interest for CO_2 sequestration. Hydromechanical numerical studies usually take the values obtained from samples tested at the laboratory as the values of the formation. However, typical laboratory tests are representative of the rock matrix, possibly damaged during coring, but not of the formation as a whole, which is always fractured. Since fractures facilitate strain, the effective formation scale value of the Young's modulus can be more than one order of magnitude smaller than that of the matrix. For example, Verdon *et al*. (2011) had to reduce the Young's modulus of the aquifer from 14.5 (value obtained from laboratory tests) to 0.5 GPa in order to adjust their model to the observed microseismicity in the Weyburn field, Saskatchewan, Canada. Though they argue that this reduction in the Young's modulus may be excessive, it is evident that laboratory tests overestimate the stiffness of the rock.

3. HYDROMECHANICAL CHARACTERIZATION TEST

3.1. TEST DESCRIPTION

We propose a test to characterize the hydromechanical parameters of the aquifer and caprock at the field scale. The test consists in injecting water at high pressure and flow rate, while monitoring fluid pressure, rock deformation and induced microseismicity (Figure 3). The injected water may also be colder than the formation, which contributes to stressing the formation. The effect of temperature is not analyzed here, but has been analyzed by Vilarrasa *et al*. (2012). The overpressure (several MPa) is proportional to the flow rate, which can become high if the aquifer transmissivity is high. The injected water can be obtained from surface sources, e.g. rivers or lakes. However, aquifer brine must be used if geochemical alteration is not desired. In this case, brine is pumped and stored at the surface prior to the injection test. Therefore, the duration of the injection will be conditioned by storage capacity.

The overpressure should be progressively increased until the elastic limit is reached and microseismicity occurs. Microseismic events can take place both in the reservoir and the caprock. Since microseismic eventss open up fractures (Guglielmi *et al*., 2008), enhancing their transmissivity, microseismicity will be beneficial while it occurs within the aquifer. However, if microseismic events occur in the caprock, they may open migration paths for CO_2. Therefore, the corresponding injection pressure must not be exceeded during the operational stage of CO_2 injection.

Instrumentation for the test consists of sensors to measure fluid pressure, vertical displacement and microseismicity. Fluid pressure and vertical displacement measurements are taken in the injection and observation wells, both in the reservoir and

the caprock (Figure 3). In the case that vertical displacement measurements are not available, strain should be measured. An array of geophones or hydrophones should be placed in the observation well at depth to detect and locate accurately microseismic events of magnitudes as low as -3. Additionally, a network of geophones in surface can complement the microseismicity measurements and help to localize the events. Microseismicity measurements are essential to guarantee the caprock integrity and avoid leakage of future CO_2 injection tests in the same site.

3.2. PROBLEM FORMULATION

3.2.1. ELASTICITY IN POROUS MEDIA

Fluid injection induces strain in the aquifer-caprock system, which is generally assumed to be elastic while failure conditions are not reached. Hooke's law gives the relationship between elastic strain and effective stress,

$$\boldsymbol{\varepsilon} = \frac{\sigma'_m}{3K}\mathbf{I} + \frac{1}{2G}\left(\boldsymbol{\sigma}' - \sigma'_m\mathbf{I}\right), \qquad (1)$$

where $\boldsymbol{\varepsilon}$ is the elastic strain tensor, $\boldsymbol{\sigma}'$ is the effective stress tensor, $\sigma'_m = \left(\sigma'_x + \sigma'_y + \sigma'_z\right)/3$ is the mean effective stress, $\mathbf{I}$ is the identity matrix, $K = E/\left(3\left(1-2\nu\right)\right)$ is the bulk modulus, $G = E/\left(2\left(1+\nu\right)\right)$ is the shear modulus, E is the Young's modulus and ν the Poisson ratio.

The coupled hydromechanical equation can be obtained from combining the flow equation (Bear, 1972) with the momentum balance, neglecting the inertial terms, considering the compatibility equations between strains and displacements and that the

volumetric strain can be expressed as the divergence of the displacement vector (Jaeger *et al*., 2007)

$$G\frac{\partial}{\partial t}\nabla^2\mathbf{u}+\left(\frac{G}{3}+K+\frac{1}{\phi\beta}\right)\frac{\partial}{\partial t}\nabla\left(\nabla\cdot\mathbf{u}\right)-\frac{1}{\phi\beta}\nabla\left(\nabla\cdot\left(\kappa\nabla h\right)\right)=\mathbf{0}, \tag{2}$$

where t is time, $\mathbf{u}$ is the displacement vector, ϕ is porosity, β is water compressibility, κ is hydraulic conductivity and h is hydraulic head.

We generalize the problem by performing a dimensional analysis. The dimensionless variables of the problem are

$$t_D=\frac{t}{t_c};\ h_D=\frac{h}{h_c};\ \mathbf{u}_D=\frac{\mathbf{u}}{u_c};\ r_D=\frac{r}{L}\ \text{and}\ \kappa_D=\frac{\kappa}{\kappa_c} \tag{3}$$

where r is the radial coordinate, L is a characteristic distance and the subscripts D and c denote dimensionless and characteristic variables, respectively. The characteristic variables can be taken as the values of each variable in the aquifer. Thus, the value of the variables in the caprock will be expressed as the ratio with respect to the value of the variable in the aquifer. The characteristic length, which is usually difficult to choose (Kopp *et al*., 2009), can be chosen as the aquifer thickness.

According to the hydraulic boundary condition, i.e. a constant flow rate, the characteristic head can be defined as

$$h_c=\frac{Q}{2\pi b_{aq}\kappa_c}, \tag{4}$$

where Q is the flow rate and b_{aq} is the aquifer thickness.

The mechanical boundary conditions of this problem are no displacement perpendicular to the bottom and outer boundary. The characteristic displacement u_c can be chosen as the vertical displacement in the aquifer induced by injection. Assuming no horizontal strain in the aquifer, it can be written as

$$u_c = h_c S_s b_{aq}, \tag{5}$$

where S_s is the specific storage coefficient.

The characteristic time can be defined from the flow equation, yielding the characteristic time of a diffusion equation

$$t_c = \frac{L^2 S_s}{\kappa_c}. \tag{6}$$

Using the dimensionless variables of Eq. (3) and the characteristic variables of Eqs. (4), (5) and (6), after some algebra, Eq. (2) can be written as

$$G' \frac{\partial}{\partial t_D} \nabla_D{}^2 \mathbf{u}_D + \left(\frac{G'}{3} + \frac{1}{Le} \right) \frac{\partial}{\partial t_D} \nabla_D (\nabla_D \cdot \mathbf{u}_D) - \frac{L}{b_{aq}} \nabla_D (\nabla_D \cdot (\kappa_D \nabla_D h_D)) = \mathbf{0}\ , \tag{7}$$

where the two dimensionless groups that govern the hydromechanical problem are

$$G' = G\phi\beta \tag{8a}$$

and

$$Le = \frac{\alpha}{\phi\beta + \alpha} \tag{8b}$$

where $\alpha = 1/K$ is rock compressibility. Note that the third term of Eq. (7) simplifies by choosing the characteristic length as the aquifer thickness. The dimensionless number

appearing in Eq. (8b) is the loading efficiency, which represents the ratio of change of fluid pressure to change of mean stress (van der Kamp and Gale, 1983; Hsieh *et al*., 1988).

3.2.2. ELASTICITY IN POROUS MEDIA WITH DILATANCY

Frictional materials often display a positive volumetric strain (increase in volume) in response to increases in deviatoric stress (Verruijt, 1969; van der Kamp and Gale, 1983). This behavior, which is not consistent with Eq. (1) is termed dilatancy (Reynolds, 1885; Houlsby, 1991). Later, we perform numerical simulations with plastic deformation including dilatancy. Still, for the sake of completeness and simplicity, here we account for dilatancy as a first approximation by adding to the volumetric strain a term that accounts for volumetric strain due to changes in deviatoric stress

$$\varepsilon_v = \frac{\sigma'_m}{K} + Dq\,, \tag{9}$$

where D is a dilatancy coefficient. Therefore, Hooke's law adopts the following form

$$\boldsymbol{\varepsilon} = \left(\frac{\sigma'_m}{3K} + \frac{D}{3}q\right)\mathbf{I} + \frac{1}{2G}\left(\boldsymbol{\sigma}' - \sigma'_m\mathbf{I}\right), \tag{10a}$$

$$\boldsymbol{\sigma}' = K\left(\varepsilon_v - D'\varepsilon_d\right)\mathbf{I} + 2G\left(\boldsymbol{\varepsilon} - \frac{\varepsilon_v}{3}\mathbf{I}\right), \tag{10b}$$

where the dilatancy parameter D' can be related to the parameters $D' = 3DG = \tan\psi$ and ψ is the dilatancy angle.

Then, we proceed in the same manner as in the previous section. But, the dimensionless equation that is obtained for the hydromechanical problem has an additional term for the dilatancy in comparison with Eq. (7)

$$G'\frac{\partial}{\partial t_D}\nabla_D{}^2\mathbf{u}_D+\left(\frac{G'}{3}+\frac{1}{Le}\right)\frac{\partial}{\partial t_D}\nabla_D\left(\nabla_D\cdot\mathbf{u}_D\right)-N_D\frac{\partial}{\partial t_D}\nabla_D\varepsilon_{dD}-\frac{L}{b_{aq}}\nabla_D\left(\nabla_D\cdot\left(\kappa_D\nabla_D h_D\right)\right)=\mathbf{0}\,, \tag{11}$$

where the dimensionless number in the dilatancy term is

$$N_D=\frac{2\pi b_{aq}k_{aq}}{Q\mu}\varepsilon_c K\tan\psi\left(1-Le\right), \tag{12}$$

where ε_c is a characteristic deviatoric strain.

The main difference between this dimensionless number and the other two is that the hydraulic variables, i.e. permeability and flow rate, appear in the dimensionless number of the dilatancy term.

3.2.3. ONSET OF MICROSEISMICITY

Induced microseismicity occurs if the stress state reaches yield conditions. To determine this, a failure criterion has to be defined. We adopt the Mohr-Coulomb failure criterion (Figure 4)

$$\tau=c'+\sigma_n'\tan\phi'\,, \tag{13}$$

where τ is the shear stress, σ_n' is the normal effective stress, c' is cohesion and ϕ' is the friction angle. Fluid pressure increases due to fluid injection, which displaces the

Mohr circle to the left. Shear failure, leading to slip along the planes of a fracture, occurs when the Mohr circle becomes tangent to the failure envelope. This can occur in a favorably oriented cohesionless preexisting fracture (Mohr circle with center *C*' in Figure 4) or in intact rock if the deviatoric stress (difference between the maximum and the minimum principal stresses) is sufficiently large to make the Mohr circle tangent to the failure envelope. Alternatively, if the least principal stress equals the rock tensile strength, σ_t', a hydrofracture will be created perpendicular to the least principal stress (Mohr circle with center *C*'' in Figure 4). If the least principal stress is horizontal, hydrofractures will be vertical, and vice versa (Klee *et al*., 2011). Generally, shear failure in preexisting fractures occur before failure of intact rock, even when they are not favorably oriented (Rutledge and Phillips, 2003).

The style of faulting is a consequence of the preexisting stress tensor. Depending on the relative magnitude of the vertical stress with respect to the two horizontal principal stresses, three cases can be distinguished: normal, strike slip and reverse faulting. Normal faulting occurs when the vertical stress is the maximum principal stress; strike slip faulting occurs when the vertical stress is the intermediate principal stress and reverse faulting occurs when the vertical stress is the minimum principal stress. The latter may take place in compressional regimes where lateral deformation is constrained in the direction perpendicular to compression. A compilation of the present-day stress field was carried out by the World Stress Map Project (Zoback, 1992). However, local variations must be expected in response to local stiffness heterogeneity. Therefore an assessment of the local initial stress tensor must be made in every case.

3.3. NUMERICAL SOLUTION

The hydromechanical characterization test is simulated using the fully coupled finite element code CODE_BRIGHT, which can handle multiphase flow, heat transfer, mass transport and deformation (Olivella *et al*., 1994, 1996). An ideal homogeneous horizontal aquifer-caprock system with the geometrical distribution of the Hontomín pilot test is considered (Figure 3). We assume that preexisting fractures are included in this equivalent continuum model. The aquifer has a thickness of 100 m, which we define as the characteristic length of the problem. The top of the aquifer is located at a depth of 1500 m. The aquifer is overlaid by a low-permeability caprock. Several thicknesses of the caprock have been considered: from 50 to 1500 m. The caprock is covered by a low shear stiffness medium, which do not need to be included in the model. For elastic hydromechanical simulations, we take advantage of radial symmetry and model an axisymmetric domain that extends laterally up to 20 km. The hydraulic boundary condition in the outer boundary is constant pressure, but the pressure buildup cone does not reach this boundary for the time scale of the test, so the model behaves as an infinitely acting aquifer. An injection well with a radius of 0.15 m is placed at the centre of the domain and the observation well is placed 50 m away. The injection flow rate is set to 120 kg/s. We have performed a sensitivity analysis of the elastic parameters in which the Young's modulus ranges from 0.1 to 50 GPa for the aquifer and from 1 to 50 GPa for the caprock, and the Poisson ratio ranges from 0.2 to 0.4 for both the aquifer and the caprock. The values of the parameters used in the simulations are summarized in Table 1. A structured mesh of quadrilateral elements has been used. The element size grows progressively from the injection well to the outer boundary. As a first step, a steady-state calculation is carried out to ensure equilibrium for the pressure and stress fields prior to injection.

Microseismicity propagation patterns are investigated by making an analogy between plastic strain and microseismic events. Since plastic strain occurs when a seism takes place, the region where seismic events would occur can be assessed by tracking the evolution of plastic strain. Thus, we simulate fluid injection using a viscoplasticity constitutive law in 3D models that represent the three possible stress regimes, i.e. normal, strike slip and reverse faulting. The details of the viscoplastic constitutive law can be found in Vilarrasa *et al*. (2010b). The geometry of these models is analogous to the axisymmetric models, but in 3D. We only model one fourth of the domain because of symmetry. The stress ratio $\sigma'_v : \sigma'_H : \sigma'_h$, where σ'_v is the vertical effective stress, σ'_H is the maximum horizontal principal effective stress and σ'_h is the minimum horizontal principal effective stress, is 1:0.65:0.4 for normal faulting, 1:1.1:0.45 for strike slip faulting and 1:1.95:1.1 for reverse faulting. The friction angle has been set to 30º for the aquifer and to 22º for the caprock.

4. RESULTS

4.1. HYDROMECHANICAL BEHAVIOUR

Fluid injection in an aquifer causes an increase in fluid pressure that reduces effective stresses, thus expanding the aquifer. As a result, the caprock is also deformed (Figure 5a). But the hydraulic pressure buildup from the aquifer into the caprock is orders of magnitude slower than in the aquifer due to the permeability contrast between the two formations. This means that the hydraulic driven overpressure only affects a few meters into the caprock. Still, significant fluid pressure changes occur throughout the caprock driven by mechanical deformation, which causes volumetric strains (i.e., changes in

porosity) (Figure 5). In fact, fluid pressure decreases in the upper part of the caprock, where the porosity increases (extension occurs). In contrast, fluid pressure increases in the parts of the caprock where the porosity decreases (compression occurs). This is because the pore space becomes smaller for a constant mass of fluid and thus fluid pressure increases.

Figure 5a displays the original and deformed form of the aquifer and caprock as a consequence of fluid injection in the aquifer. Vertical displacement displays a shape similar to that of fluid overpressure at the top of the aquifer, which decreases logarithmically with distance. However, vertical displacement becomes smoother at the top of the caprock. The uplift at the top of the aquifer generates compression in the lower part of the caprock close to the injection well, so fluid pressure increases. However, extensions appear at the top of the caprock close to the well, which increases the pore volume and thus fluid pressure decreases (Figure 5b). This leads to a reverse-water level fluctuation, which is well-documented in confined aquifers. When fluid is pumped, hydraulic heads in adjacent aquitards rise after pumping starts (Rodrigues, 1983; Hsieh, 1996; Kim and Parizek, 1997). This phenomenon is known as "reverse-water level fluctuation" or "Noordbergum effect", because it was observed for the first time in the village of Noordbergum, the Netherlands (Verruijt, 1969). The opposite occurs far from the injection well, i.e. extensions at the lower part of the caprock and compressions at its top. However, these are small compared to those close to the well.

Fluid injection produces both a vertical and a horizontal displacement of the aquifer. The aquifer is horizontally displaced away from the injection well (Figure 6a) and pushed upwards (Figure 6b). The horizontal strain can even become negative at a certain distance from the well. The deformation of the aquifer produces deformation of

the caprock, with the condition that displacements are continuous at the aquifer-caprock interface. The caprock acts as a spring, dissipating the deformation of the aquifer. Hence, horizontal strain decreases rapidly at the lower part of the caprock (Figure 6a) and vertical strain is negative in the caprock (Figure 6b), which means that its thickness becomes smaller. The high gradient of horizontal strain at the aquifer-caprock contact suggests that relative displacements between the two formations might occur in the presence of a clay-rich layer with a low friction angle (see Figure 2). If this occurred, microseismic events would be triggered. Here we focus on the interaction between the aquifer and the caprock. At the bottom of the aquifer, we have assumed, for simplicity, a boundary with no displacement perpendicular to it. In reality, this boundary would present some resistance to shear and compression, so the curves would be more symmetrical with respect to the middle of the aquifer.

4.2. SENSITIVITY ANALYSIS

4.2.1. AQUIFER

The mechanical properties of the rocks that form the reservoir and the caprock in potential CO_2 storage sites are highly uncertain (recall Section 2). We analyze the sensitivity of pressures and displacements to the mechanical properties within each geological formation separately. We start by varying the mechanical properties of the aquifer while maintaining those of the caprock constant. The ratio of caprock to aquifer thickness is set to 2.

Figure 7 displays the dimensionless overpressure and vertical displacement as a function of the dimensionless group of the volumetric strain term $\Gamma_{aq} = G'_{aq}/3 + 1/Le_{aq}$

(second term in the left hand side of Eq. (7)) at the top of the aquifer and the top of the caprock. The results correspond to a dimensionless time equal to 1 and a dimensionless distance from the injection well of 0.5. The most relevant variables in this analysis are listed in Table 2. The dimensionless group of the volumetric strain term Γ_{aq} is a measure of the stiffness of the rock. High values of Γ_{aq} indicate a stiff rock and low values of Γ_{aq} indicate a soft rock. Dimensionless fluid overpressure in the aquifer is approximately equal to 1 and the effect of the Poisson ratio has little effect, showing that the variability is captured by the dimensional analysis (Figure 7a). The reverse-water level fluctuation is more pronounced for soft aquifers, which can lead to a fluid pressure drop at the top of the caprock almost as high as the overpressure in the aquifer. However, fluid pressure variations at the top of the caprock are almost negligible when injecting in very stiff aquifers. Note that the curves of pressure drop at the top of the caprock coincide regardless of the Poisson ratio. This means that the Poisson ratio of the aquifer has no effect on the overpressure at the top of the caprock when plotting the results as a function of the dimensionless group of the volumetric strain term Γ_{aq}.

Similarly, the dimensionless vertical displacement at the top of the aquifer is independent of the aquifer Poisson ratio when plotted as a function of the dimensionless group of the volumetric strain term Γ_{aq} (Figure 7b). However, it has some effect at the top of the caprock, which can help to characterize the aquifer's Poisson ratio. The dimensionless vertical displacement is small for very soft aquifers. It increases both at the top of the aquifer and the caprock as the aquifer becomes stiffer, until it reaches a maximum and then decreases (Figure 7b). This behavior can be explained by the fact that as the aquifer becomes stiffer, its loading efficiency (Eq. (8b)) decreases. The loading efficiency measures the part of a load that is taken by the pore-water with

respect to the solid skeleton of a soil or rock. While water takes almost all the load in soft soils, stiff rocks have a compressibility comparable to that of water multiplied by porosity, so the load distributes between the solid skeleton and the water. Thus, the dimensionless vertical displacement presents its maximum when a non-negligible part of the load is taken by the solid skeleton of the porous media. The difference between the vertical displacement at the top of the caprock and at the top of the aquifer is the amount of displacement absorbed by the caprock.

Field measurements of fluid pressure and vertical displacement can be used to characterize the mechanical properties of the aquifer and caprock. Figure 8 shows possible combinations of fluid overpressure and vertical displacement at the top of the aquifer as a function of the aquifer mechanical properties at a dimensionless distance of 0.5 from the injection well. Thus, the mechanical properties of the aquifer can be determined by introducing field measurements (fluid overpressure and vertical displacement) in Figure 8.

The proposed test can also be used as a conventional hydraulic test to characterize the hydraulic properties of the aquifer. The interpretation of fluid pressure evolution of the injection test gives the aquifer transmissivity and storage coefficient (Cooper and Jacob, 1946). The mechanical properties of the aquifer have little effect on fluid overpressure evolution in the aquifer when plotted versus dimensionless time (Figure 9a). In actual dimensions, pressure buildup is delayed in soft aquifers and for small Poisson ratios because of their higher storativity. On the other hand, pressure drop at the top of the caprock becomes bigger for softer aquifers (Figure 9b). Note the difference between hydromechanical simulations and a purely hydraulic simulation (denoted by *H* in Figure 9). Although the difference is small in the aquifer, the reverse-water level fluctuation

does not occur in the caprock. It is clear that hydromechanical simulations are essential for understanding pressure evolution in the caprock during fluid injection. Moreover, these results suggest that pressure evolution in the caprock can be used to derive its mechanical properties.

4.2.2. CAPROCK

We now analyze the sensitivity of the solution to caprock mechanical properties while maintaining constant those of the aquifer to test whether they can be derived from the measured response. The effect of the caprock thickness is also examined.

Figure 10 displays the dimensionless overpressure at the top of the aquifer as a function of the dimensionless group of the volumetric strain term Γ_{cap} for a dimensionless time equal to 1 and a dimensionless distance from the injection well of 0.5. The overpressure increases slightly with the caprock stiffness. This was also observed by Yin *et al*. (2009), but considering that the reservoir is closed, i.e. surrounded by a low-permeability formation. The thickness of the caprock has a greater effect in stiff caprocks than in soft ones. The thicker the caprock, the higher the overpressure at the top of the aquifer. This is because stiff thick caprocks may control the rigidity of the aquifer-caprock system, increasing the stiffness of the aquifer. This affects the storage coefficient, reducing it and therefore the pressure buildup occurs faster than with a thin soft caprock.

The variation of the mechanical properties and thickness of the caprock has a greater effect on the vertical displacement (Figure 11) than on the overpressure (Figure 10). Although the caprock Poisson ratio has a negligible effect both on fluid overpressure

and vertical displacement (results not shown), the stiffness of the caprock does have an effect. Vertical displacement at the top of the aquifer decreases as the caprock becomes stiffer and thicker because they increase the bending moment of the caprock, which opposes to vertical displacement. In contrast, vertical displacement at the top of the caprock increases with the caprock stiffness, because the stiffer the caprock, the lesser deformation it absorbs. However, the deformation absorbed by the caprock increases with its thickness, thus decreasing vertical displacement. This leads to the extreme case of thick soft caprocks that can yield subsidence at the top of the caprock (Figure 11). The dashed lines reproduce the vertical displacement of a caprock that reaches the surface at the depths of the top of all the considered caprocks. The vertical displacement is similar at all depths when the caprocks are soft. However, the deformation within the caprock is significantly different for stiff caprocks, in part because the vertical displacement at the top of the aquifer is controlled by the caprock thickness.

4.3. INDUCED MICROSEISMICITY ANALYSIS

4.3.1. ELASTIC MODELS

Figure 12 displays the mobilized friction angle at the top of both the aquifer and the caprock as a function of the dip angle of a preexisting cohesionless fracture for a dimensionless time equal to 1 and an axisymmetric stress tensor with a vertical maximum principal stress. Stiffness of either aquifer or caprock has little effect on the mobilized friction angle. However, soft aquifers yield a somewhat higher mobilized friction angles than stiff aquifers, reflecting that the increased expansion implies a somewhat larger reduction in horizontal effective stresses. The effect of the stiffness of

the caprock is even smaller. The maximum mobilized friction angles at the top of the aquifer are in the order of 25-30° for steep fractures with dip angles around 60°; but only in the order of 15-17° for fractures with dip angles around 55° at the top of the caprock.

Figure 13 shows the mobilized friction angle at the top of the aquifer as a function of time. Soft aquifers yield a higher mobilized friction angle than stiff aquifers for early times. However, the situation is reverted for late times of injection. The mobilized friction angles increases linearly with the logarithm of time in stiff aquifers, which may lead to failure conditions in long injection periods, as pressure grows also linearly with the logarithm of time. Notice that this is not the situation for supercritical CO_2, with a viscosity much smaller than that of water, which causes pressure to drop as the CO_2 plume grows (Vilarrasa *et al.*, 2010b). The effect of the Poisson ratio is small but non-negligible because the changes in horizontal stresses induced by fluid injection depend on the Poisson ratio (e.g. Rutqvist, 2012). The vertical expansion associated to fluid injection also causes a reduction in horizontal effective stresses that is proportional to the Poisson ratio, which leads to an increase in the mobilized friction angle with the Poisson ratio.

The fact that the dip angle corresponding to the maximum mobilized friction angle varies from the aquifer to the caprock (Figure 12) is not a coincidence. In fact, the dip angle corresponding to the maximum mobilized friction angle can be obtained geometrically, as shown in Figure 14, and is equal to

$$\delta = \frac{\pi}{4} + \frac{\phi'_{mob}}{2}, \tag{14}$$

where δ is the dip (angle with respect to the horizontal) of the critically oriented fracture and ϕ'_{mob} is the mobilized friction angle. The mobilized friction angle is such that the Mohr-Coulomb envelope is tangent to the Mohr circle. The pole (denoted by *P* in Figure 14) of the Mohr circle coincides with the minimum principal stress when the maximum principal stress is vertical. Though fluid injection produces a slight rotation of the stress tensor, it can be neglected because pressure variations are relatively small. By definition, the stress state at any plane is obtained by intersecting the Mohr circle with the straight line drawn from the pole with the same orientation as the plane. Thus, a simple geometric derivation leads to Eq. (14) for the dip of the critically oriented fracture. Therefore, the higher the mobilized friction angle, the steeper the critically oriented fracture. Replacing the maximum mobilized friction angles in the aquifer and caprock in Eq. (14) gives the dip angles of the critically oriented fractures for triggering induced microseismicity shown in Figure 12.

4.3.2. PLASTIC MODELS

The type of faulting is determined by the stress tensor. In a normal faulting stress regime, rock fails along steep shear planes (Figure 15b, c). The numerical model reproduces very well the plastic propagation, which follows an angle equal to $\pi/4+\phi'/2$ (Figure 15c). Note that this is the same stress regime as the one analyzed in the previous section. The fact that the rock has some cohesion does not affect the angle in which shear occurs because the proportions between the triangles in the Mohr-Coulomb failure analysis are maintained (Figure 15a).

In a strike slip stress regime, shear planes are vertical (Figure 16b). The situation of the pole is somewhat arbitrary in this stress regime. The pole coincides with the maximum horizontal principal effective stress in Figure 16a. However, if the pole had coincided with the minimum horizontal principal effective stress, the angle with respect to this direction in which shear occurs would have been the complementary of the one shown in Figure 16a, i.e., $\pi/4+\phi'/2$, leading to the same orientation of the shear plane shown in Figure 16b. Numerical results show that plastic deformation is indeed vertical and perpendicular to the maximum horizontal stress (Fig. 16c). The region with plastic deformations is relatively wide because viscoplasticity regularizes and does not localize the failure mechanism.

In a reverse faulting stress regime, the rock fails along shallowly dipping shear planes (Figure 17b, c). In this case, the pole coincides with the maximum horizontal principal effective stress and thus the failure plane (line *P*-*A*) presents a dip angle equal to $\pi/4-\phi'/2$, which is lower than 45º (Figure 17a). Figure 17c shows that indeed plastic deformations occur subhorizontally. Microseismicity monitoring can thus help in confirming the initial stress tensor at the site by identifying the propagation pattern with one of these types of faulting.

Figure 18 displays the stress trajectories (deviatoric versus mean effective stresses) for the three stress regimes at a point of the caprock placed 25 m away from the top of the injection well in all directions. All the trajectories start inside the failure envelope (elastic behavior). However, the trajectories shift to the left because of fluid pressure increase once fluid injection starts. Finally, all trajectories touch the failure envelope, meaning that the caprock yields and microseismic events occur.

5. DISCUSSION

We propose a hydromechanical characterization test that will permit estimating representative values of the hydromechanical properties at the field scale. These values can be used as input data in numerical models, to facilitate numerical interpretation of measured data.

Not only does this injection test give information on the hydraulic properties of the aquifer, but also on the hydraulic properties of the caprock and boundaries. A first estimate of the caprock permeability can be obtained from Earth tide analysis by monitoring fluid pressure fluctuations and Earth tide dilation prior to injection (Hsieh *et al.*, 1987). Furthermore, the injection will last several hours and up to a few days, so the drawdown evolution curve will suffer several changes in its slope in a semilog plot. These changes in slope yield further information on the permeability of the caprock (Hantush, 1956; Neuzil, 1986) or the existence of faults that may act either as a flow barrier or constant head boundaries (Hsieh and Bredehoeft, 1981). The actual nature (barrier or conduits) of these faults can be determined if the pressure buildup cone (Vilarrasa *et al*., 2010a) reaches them. If faults are detected, more realistic models of the site need to be performed and calibrated including heterogeneities that have not been included here. Apart from this, permeability can be enhanced if the aquifer fractures open up (triggering microseismic events) as a response to high pressure injection (Vilarrasa *et al*., 2011a), which would reduce the slope of the drawdown evolution curve in the semilog plot. This can be accommodated in numerical models by using stress dependent permeability models.

Additionally, this field test can be used as a means of measuring the caprock stability to fluid injection at high pressure. We suggest injecting water, but CO_2 can be used as

well, because it has been observed that water and CO_2 have a similar effect on fracture stimulation (Verdon *et al.*, 2010). However, the risk of inducing microseismic events increases with time when injecting water (recall Figure 13), but is highest at the beginning of injection when injecting CO_2 (Vilarrasa *et al.*, 2010b). Microseismicity monitoring should allow to locate the induced microseismic events (Xuan and Sava, 2010). The minimum detectable magnitude depends on the depth at which an array of geophones can be placed. Small events, of magnitude ranging from -3 to -2, can be detected only if the geophones are placed in a nearby borehole at a similar depth than the aquifer-caprock system (Moeck *et al.*, 2009; Bohnhoff *et al.*, 2010). The fracture slip likelihood as a function of fracture orientation can be determined from a slip tendency analysis (Segall and Fitzgerald, 1998; Moeck and Backers, 2011). The mobilized friction angle is higher in the aquifer than in the caprock (Figure 12) because the overpressure induced by injection translates the Mohr circle to the left (see Figure 4). However, the likelihood of microseismic events occurrence depends on the actual friction angle of each formation. In fact, as shown in Figure 2, caprock materials often display low-friction angles, so that shear failure can occur in critically oriented fractures.

The onset of microseismicity in the caprock can be used to define the maximum sustainable injection pressure. The value of this sustainable pressure will be a measure of the suitability of a specific site for permanent CO_2 storage. Low values of the maximum sustainable injection pressure are indicative that the site can undergo large plastic deformations (Vilarrasa *et al.*, 2011b) and may reactivate faults (Rutqvist *et al.*, 2008) which might facilitate CO_2 migration towards shallow depths.

The initial stress tensor plays an important role in assessing the suitability of a specific site for permanent CO_2 storage. Shear planes are subhorizontal in reverse faulting stress regime, but they are subvertical in normal faulting stress regime, as shown theoretically and numerically (Figures 15 and 17). Thus, it is more likely that the CO_2 finds a migration path that crosses the whole caprock in a normal faulting than in a reverse faulting stress regime. But, strike slip stress regime seems even more unfavorable, because shear planes are vertical (Figures 16). The intensity of earthquakes also depends on the stress regime. Schorlemmer *et al*. (2005) found that the largest earthquakes occur in reverse faulting stress regime; normal faulting stress regime presents a larger proportion of small earthquakes and strike slip faulting stress regime has an intermediate behavior. Hence, the propensity for large earthquakes in a reverse faulting stress regime counterbalances the less unfavorable orientation of shear planes. However, the stress regime should not be a limiting factor if a careful monitoring of the hydromechanical response is performed, as evidenced in In Salah (Rutqvist, 2012), where a strike slip stress regime exists. In the Hontomín site, according to the World Stress Map, the geological indicators suggest a normal faulting stress regime. However, there is an inactive strike slip fault nearby. Once the drilling operations start, the actual stress regime will be determined and the site could be assessed.

The initial stress tensor can be determined from observation of breakouts, tensile fractures and induced hydrofractures in wells (Zoback *et al*., 2003). Alternatively, the observation of similar patterns in microseismic events (e.g. doublets, multiplets, wavelength, slip direction) can give clues to determine the stress tensor (Rubin *et al*., 1999; Tezuka and Niitsuma, 2000; Pytharouli *et al*., 2011). The stress tensor determination is not easy and may change with depth (Plenefisch and Bonjer, 1997; Klee *et al*., 2011). Nevertheless, the magnitude and orientation of the principal stresses

should be, at least, delimited in order to have some confidence on the existing stress tensor and how far or close it is from failure. The latter can be assessed by the interpretation of the proposed hydromechanical characterization test.

The dimensional analysis of the hydromechanical equations shows that the problem is governed by two parameters: the loading efficiency and another that can be expressed as a function of the loading efficiency and the Poisson ratio as

$$G' = \left(\frac{1}{Le} - 1 \right) \frac{3(1-2\nu)}{2(1+\nu)}. \tag{15}$$

Note that the ratio where the Poisson ratio appears is the shear to bulk modulus ratio, i.e. G/K. The dimensionless curves of fluid pressure and vertical displacement as a function of these parameters permit the estimation of the mechanical properties of the aquifer and caprock. The dimensional analysis considers the possibility that the rock presents dilatancy. Its effect should be considered as a possible contributing term when analyzing hydromechanical measurements. Though real potential storage sites will present a complex geometry, each site may be idealized as one similar to the ones studied here. Thus, the results presented here will permit to gain insights on the relevant hydromechanical processes occurring in each site.

One of the most surprising hydromechanical processes occurring during fluid injection in an aquifer overlaid by a caprock is the reverse-water level fluctuation. Hydromechanical coupling is required to simulate this effect (see Figure 9). We use this effect, which is more pronounced in soft aquifers, to determine the geomechanical properties of the rocks. This effect can be difficult to measure in situ if the aquifer is stiff because it will lead to small fluid pressure changes, which will only be detected by very precise measuring equipment.

Vertical displacement is not easy to measure in deep boreholes. Strain measurements with fiber optic may be an option. However, the actual nature of the measurement is often unclear: Is it measuring the strain of the rock? Or is it measuring that of the casing? The measuring equipment will be embedded in the cement between the casing and the rock, which are of different stiffness, and thus deform differently. If the cement-rock contact becomes a sliding surface, then the measuring equipment will measure the casing strain. This would give the impression that the rock is much stiffer than it actually is. However, the combined interpretation of fluid pressure and vertical displacement measurements will help in deciding whether some measurements are or not representative of the aquifer or caprock. Overall, the hydromechanical parameters of the aquifer and caprock at the field scale can be estimated from the interpretation of the proposed hydromechanical characterization field test.

6. CONCLUSION

We propose a hydromechanical characterization test for determining the aquifer and caprock hydromechanical properties at the field scale. Additionally, the maximum sustainable CO_2 injection pressure can be determined by monitoring induced microseismicity. This will help to assess the suitability of specific sites for permanent CO_2 storage in deep saline formations.

We obtain the parameters that govern the problem through a dimensional analysis. We present the dimensionless overpressure and vertical displacement as a function of these parameters, which yields a family of curves for several Poisson ratios. Except for the vertical displacement at the top of the caprock, which depends on the Poisson ratio, all

the curves collapse in one single curve when plotting the results as a function of the dimensionless group of the volumetric strain term Γ_{aq}. Not only do these curves show the behavior of the aquifer-caprock system when injecting a fluid, but also can they be used for parameter estimation from field measurements.

The coupled hydromechanical simulations of fluid injection show a reverse-water level fluctuation in the caprock, i.e. fluid pressure drops in the caprock when injecting in the subjacent aquifer. This phenomenon cannot be simulated with purely hydraulic simulations. Thus, coupled hydromechanical simulations should be performed when seeking understanding of caprock processes during fluid injection.

Induced microseismicity in the caprock is a source of concern. The mobilized friction angle is much lower in the caprock than in the aquifer. However, clay-rich materials, typical of caprocks, usually display low-friction angles, especially in the direction parallel to bedding. Thus, microseismicity monitoring is required to control and gain confidence on the caprock integrity.

ACKNOWLEDGEMENTS

V.V. wishes to acknowledge the Spanish Ministry of Science and Innovation (MCI), through the "Formación de Profesorado Universitario" Program, and the "Colegio de Ingenieros de Caminos, Canales y Puertos – Catalunya" for their financial support. This work has been funded by Fundación Ciudad de la Energía (Spanish Government) (www.ciuden.es) through the project ALM/09/018 and by the European Union through the "European Energy Programme for Recovery" and the Compostilla OXYCFB300 project. We also want to acknowledge the financial support received from the

‘MUSTANG’ (www.co2mustang.eu) and ‘PANACEA’ (www.panacea-co2.org) projects (from the European Community’s Seventh Framework Programme FP7/2007-2013 under grant agreements nº 227286 and nº 282900, respectively).

REFERENCES

Abousleiman YN, Hoang SK, Tran MH. Mechanical characterization of small shale samples subjected to fluid exposure using the inclined direct shear testing device. *International Journal of Rock Mechanics and Mining Sciences* 2010, **47**: 355-367.

Barton N, Bandis S, Bakhtar K. Strength, deformation and conductivity coupling of rock joints. *International Journal of Rock Mechanics and Mining Sciences & Geomechical Abstracts* 1985, **22 (3)**: 121–140.

Bear J (ed.). *Dynamics of fluids in porous media*. Elsevier, New York, 1972.

Bohnhoff M, Zoback MD, Chiaramonte L, Gerst JL, Gupta N. Seismic detection of CO_2 leakage along monitoring wellbores. *International Journal of Greenhouse Gas Control* 2010, **4 (4)**: 687–697.

Cai M, Morioka H, Kaiser PK, Tasaka Y, Kurose H, Minami M, Maejima T. Back-analysis of rock mass strength parameters using AE monitoring data. *International Journal of Rock Mechanics and Mining Sciences* 2007, **44**: 538-549.

Cappa F, Rutqvist J. Modeling of coupled deformation and permeability evolution during fault reactivation induced by deep underground injection of CO_2. *International Journal of Greenhouse Gas Control* 2011a, **5 (2)**: 336-346.

Cappa F, Rutqvist J. Impact of CO_2 geological sequestration on the nucleation of earthquakes. *Geophysical Research Letters* 2011b, **38**, L17313, doi: 10.1029/2011GL048487.

Cappa F, Rutqvist J. Seismic rupture and ground accelerations induced by CO_2 injection in the shallow crust. *Geophysical Journal International* 2012, **190**: 1784-1789.

Carrera J, Silva O, Rötting T, Carbonell R, Vilarrasa V, Pérez-Estaún A, CIUDEN's research group. Characterization and working programme of Hontomín CO_2 injection site (Spain). Monitoring, hydrogeochemical characterization and injection tests. *6th Trondheim Carbon, Capture and Sequestration Conference*, 14-16 June 2011, Trondheim, Norway.

Chiaramonte L, Zoback MD, Friedmann J, Stamp V. Seal integrity and feasibility of CO_2 sequestration in the Teapot Dome EOR pilot: geomechanical site characterization. *Environmental Geology* 2008, **54**: 1667-1675.

Cooper HH, Jacob CE. A generalized graphical method for evaluating formation constants and summarizing well field history. *Am. Geophys. Union Trans*. 1946, **27**: 526–534.

Dehandschutter B, Vandycke S, Sintubin M, Vandenberghe N, Wouters L. Brittle fractures and ductile shear bands in argillaceous sediments: inferences from Oligocene Boom Clay (Belgium). *Journal of Structural Geology* 2005, **27**: 1095–1112.

Dodds KJ, Dewhurst DN, Siggins AF, Ciz R, Urosevic M, Gurevich B, Sherlock DH. Experimental and theoretical rock physics research with application to reservoirs,

seals and fluid processes. *Journal of Petroleum Science and Engineering* 2007, **57**: 16–36.

Eseme E, Urai JL, Krooss BM, Littke R. Review of mechanical properties of oil shales: Implications for exploitation and basin modelling. *Oil Shale* 2007, **24 (2)**: 159–174.

Ferronato M, Gambolati G, Janna C, Teatini P. Numerical modelling of regional faults in land subsidence prediction above gas/oil reservoirs. *International Journal for Numerical and Analytical Methods in Geomechanics* 2008, **32**: 633-657.

Ferronato M, Gambolati G, Janna C, Teatini P. Geomechanical issues of anthropogenic CO_2 sequestration in exploited gas fields. *Energy Conversion & Management* 2010, **51**: 1918–1928.

François B, Laloui L, Laurent C. Thermo-hydro-mechanical simulation of ATLAS in situ large scale test in Boom Clay. *Computers and Geotechnics* 2009, **36**: 626–640.

Gens A, Vaunat J, Garitte B, Wileveau Y. In situ behaviour of a stiff layered clay subject to thermal loading: observations and interpretation. *Géotechnique* 2007, **57 (2)**: 207–228.

Giraud A, Rousset G. Time-dependent behaviour of deep clays. *Engineering Geology* 1996, **41**: 181–195.

Goodman, RE (ed.). *Introduction to Rock Mechanics*. John Wiley and Sons, New York, 1989.

Guglielmi Y, Cappa F, Amitrano D. High-definition analysis of fluid-induced seismicity related to the mesoscale hydromechanical properties of a fault zone. *Geophysical Research Letters* 2008, **35**, L06306, doi:10.1029/2007GL033087.

Hantush MS. Analysis of data from pumping tests in leaky aquifers. *Transactions American Geophysical Union* 1956, **37 (6)**: 702–714.

Heap MJ, Faulkner DR, Meredith PG, Vinciguerra S. Elastic moduli evolution and accompanying stress changes with increasing crack damage: implications for stress changes around fault zones and volcanoes during deformation. *Geophysical Journal International* 2010, **183**: 225-236.

Houlsby GT. How the dilatancy of soils affects their behaviour. *10th European Conference on Soil Mechanics and Foundation Engineering*, 28 May, 1991, Florence, Italy, Report Number OUEL 1888/91.

Hsieh PA, Bredehoeft JD. A reservoir analysis of the Denver earthquakes: A case of induced seismicity. *Journal of Geophysical Research* 1981, **86 (B2)**: 903-920.

Hsieh PA, Bredehoeft JD, Farr JM. Determination of aquifer transmissivity from earth tide analysis. *Water Resources Research* 1987, **23 (10)**: 1824-1832.

Hsieh PA, Bredehoeft JD, Rojstaczer SA. Response of well aquifer systems to earth tides: Problem revisited. *Water Resources Research* 1988, **24 (3)**: 468-472.

Hsieh PA. Deformation-induced changes in hydraulic head during ground-water withdrawal. *Ground Water* 1996, **34 (6)**: 1082-1089.

Hu DW, Zhou H, Zhang F, Shao JF. Evolution of poroelastic properties and permeability in damaged sandstone. *International Journal of Rock Mechanics and Mining Sciences* 2010, **47**: 962-973.

Jaeger JC, Cook NGW, Zimmerman RW (ed.). *Fundamentals of rock mechanics*. 4th Edition, Wiley-Blackwell, Oxford, 2007.

Kikuta K, Hongo S, Tanase D, Ohsumi T. Field test of CO_2 injection in Nagaoka, Japan. *In: Proceedings of the 7th Int. Conf. on Greenhouse Gas Control Technologies, September 2004, Vancouver, Canada*, 1367-1372.

Kim J-M, Parizek RR. Numerical simulation of the Noordbergum effect resulting from groundwater pumping in a layered aquifer system. *Journal of Hydrology* 1997, **202**: 231-243.

Klee G, Bunger A, Meyer G, Rummel F, Shen B. In situ stresses in borehole Blanche-1/South Australia derived from breakouts, core discing and hydraulic fracturing to 2 km depth. *Rock Mechanics Rock Engineering* 2011, **44**: 531-540.

Kopp A, Class H, Helmig R. Investigation on CO_2 storage capacity in saline aquifers Part 1. Dimensional analysis of flow processes and reservoir characteristics. *International Journal of Greenhouse Gas Control* 2009, **3**: 263–276.

Ledesma A, Gens A, Alonso EE. Parameter and variance estimation in geotechnical backanalysis using prior information. *International Journal for Numerical and Analytical Methods in Geomechanics* 1996, **20**: 119-141.

Mallikamas W, Rajaram H. On the anisotropy of the aperture correlation and effective transmissivity in fractures generated by sliding between identical self-affine surfaces. *Geophysical Research Letters* 2005, **32**, L11401, doi: 10.1029/2005GL022859.

Mazzoldi A, Rinaldi AP, Borgia A, Rutqvist J. Induced seismicity within geologic carbon sequestration projects: Maximum earthquake magnitude and leakage potential. *International Journal of Greenhouse Gas Control* 2012, **10**: 434-442.

Mertens J, Bastiaens W, Dehandschutter B. Characterisation of induced discontinuities in the Boom Clay around the underground excavations (URF, Mol, Belgium). *Applied Clay Science* 2004, **26**: 413-428.

Michael K, Golab A, Shulakova V, Ennis-king J, Allinson G, Sharma S, Aiken T. Geological storage of CO_2 in saline aquifers – A review of the experience from existing storage operations. *International Journal of Greenhouse Gas Control* 2010, **4**: 659–667.

Miller SA, Collettini C, Chiaraluce L, Cocco M, Barchi M, Kaus BJP. Aftershocks driven by a high-pressure CO_2 source at depth. *Nature* 2004, **427**: 724-727.

Moeck I, Kwiatek G, Zimmermann G. Slip tendency analysis, fault reactivation potential and induced seismicity in a deep geothermal reservoir. *Journal of Structural Geology* 2009, **31**: 1174-1182.

Moeck I, Backers T. Fault reactivation potential as a critical factor during reservoir stimulation. *First Break* 2011, **29**: 73:80.

Neuzil CE. Groundwater flow in low-permeability environments. *Water Resources Research* 1986, **22 (8)**: 1163-1195.

Olivella S, Carrera J, Gens A, Alonso EE. Non-isothermal multiphase flow of brine and gas through saline media. *Transport In Porous Media* 1994, **15**: 271–93.

Olivella S, Gens A, Carrera J, Alonso EE. Numerical formulation for a simulator (CODE_BRIGHT) for the coupled analysis of saline media. *Eng. Computations* 1996, **13**: 87–112.

Ortega JA, Ulm F-J, Abousleiman Y. The effect of particle shape and grain-scale properties of shale: A micromechanics approach. *International Journal for Numerical and Analytical Methods in Geomechanics* 2010, **34**: 1124-1156.

Phillips WS, Rutledge JT, House LS, Fehler MC. Induced microearthquake patterns in hydrocarbon and geothermal reservoirs: six case studies. *Pure and Applied Geophysics* 2002, **159**: 345–369.

Plenefisch T, Bonjer K-P. The stress field in the Rhine Graben area inferred from earthquake focal mechanisms and estimation of frictional parameters. *Tectonophysics* 1997, **275**: 71-97.

Pytharouli SI, Lunn RJ, Shipton ZK, Kirkpatrick JD, do Nascimento AF. Microseismicity illuminates open fractures in the shallow crust. *Geophysical Research Letters* 2011, **38**, L02402, doi:10.1029/2010GL045875.

Reynolds O. On the dilation of media composed of rigid particles in contact, with experimental illustrations. *Phil. Mag*. 1885, **20**: 469-481.

Rimmelé G, Barlet-Gouédard V, Renard F. Evolution of the petrophysical and mineralogical properties of two reservoir rocks under thermodynamic conditions relevant for CO_2 geological storage at 3 km depth. *Oil and Gas Science and Technology* 2009, **65**: 565–580.

Rodrigues JD. The Noordbergum effect and characterization of aquitards at the Rio Maior Mining Project. *Ground Water* 1983, **21 (2)**: 200-207.

Rubin AM, Gillard D, Got J-L. Streaks of microearthquakes along creeping faults. *Nature* 1999, **400**: 635-641.

Rutledge JT, Phillips WS. Hydraulic stimulation of natural fractures as revealed by induced microearthquakes, Carthage Cotton Valley gas field, east Texas. *Geophysics* 2003, **68 (2)**: 441-452.

Rutqvist, J. The geomechanics of CO_2 storage in deep sedimentary formations. *Geotechnical and Geology Engineering* 2012, doi: 10.1007/s10706-011-9491-0.

Rutqvist J, Birkholzer JT, Cappa F, Tsang C-F. Estimating maximum sustainable injection pressure during geological sequestration of CO_2 using coupled fluid flow and geomechanical fault-slip analysis. *Energy Conversion & Management* 2007, **48**: 1798–1807.

Rutqvist J, Birkholzer JT, Tsang C-F. Coupled reservoir-geomechanical analysis of the potential for tensile and shear failure associated with CO_2 injection in multilayered reservoir-caprock systems. *International Journal of Rock Mechanics and Mining Sciences* 2008, **45**: 132-143.

Rutqvist J, Vasco DW, Myer L. Coupled reservoir-geomechanical analysis of CO_2 injection and ground deformations at In Salah, Algeria. *International Journal of Greenhouse Gas Control* 2010, **4 (*2*)**: 225–230.

Saurot J, Molez L, Guéguen Y, Hoteit N. Shale dynamic properties and anisotropy under triaxial loading: Experimental and theoretical investigations. *Physics and Chemistry of the Earth* 2007, **32**: 896-906.

Schorlemmer D, Wiemer S, Wyss M. Variations in earthquake-size distribution across different stress regimes. *Nature* 2005, **437**: 539-542.

Segall P, Fitzgerald SD. A note on induced stress changes in hydrocarbon and geothermal reservoirs. *Tectonophysics* 1998, **289**: 117-128.

Shalabi FI, Cording EJ, Al-Hattamleh OH. Estimation of rock engineering properties using hardness tests. *Engineering Geology* 2007, **90**: 138–147.

Smith SA, McLellan P, Hawkes C, Steadman EN, Harju JA. Geomechanical testing and modelling of reservoir and cap rock integrity in an acid gas EOR/sequestration project, Zama, Alberta, Canada. *Energy Procedia* 2009, **1**: 2169-2176.

Soltanzadeh H, Hawkes CD. Assessing fault reactivation tendency within and surrounding porous reservoirs during fluid production or injection. *International Journal of Rock Mechanics and Mining Sciences* 2009, **46**: 1-7.

Streit JE, Hillis RR. Estimating fault stability and sustainable fluid pressures for underground storage of CO_2 in porous rock. *Energy* 2004, **29**: 1445-1456.

Tezuka K, Niitsuma H. Stress estimated using microseismic clusters and its relationship to the fracture system of the Hijiori hot dry rock reservoir. *Engineering Geology* 2000, **56**: 47-62.

Thury M. The characteristics of the Opalinus Clay investigated in the Mont Terri underground rock laboratory in Switzerland. *C. R. Physique* 2002, **3**: 923–933.

van der Kamp G, Gale JE. Theory of earth tide and barometric effects in porous formations with compressible grains. *Water Resources Research* 1983, **19 (2)**: 538-544.

Vardakos SS, Gutierrez MS, Barton NR. Back-analysis of Shimizu No. 3 by distinct element modeling. *Tunnelling and Underground Space Technology* 2007, **22**: 401-413.

Vasco DW, Rucci A, Ferretti A, Novali F, Bissell C, Ringrose PS, Mathieson AS, Wright IW. Satellite-based measurements of surface deformation reveal fluid flow associated with the geological storage of carbon dioxide. *Geophysical Research Letters* 2010, **37**, L03303, doi:10.1029/2009GL041544.

Verdon JP, Kendall JM, Maxwell SC. A comparison of passive seismic monitoring of fracture stimulation due to water versus CO_2 injection. *Geophysics* 2010, **75**, MA1–MA7.

Verdon JP, Kendall J-M, White DJ, Angus DA. Linking microseismic event observations with geomechanical models to minimise the risks of storing CO_2 in geological formations. *Earth and Planetary Science Letters* 2011, **305**: 143-152.

Verruijt A. *Elastic storage of aquifers*. In: Flow through porous media. Edited by R.J.M. de Wiest. Academic Press, New York 1969. pp. 331-376.

Vidal-Gilbert S, Tenthorey E, Dewhurst D, Ennis-King J, van Ruth P, Hillis R. Geomechanical analysis of the Naylor Field, Otway Basin, Australia: Implications for CO_2 injection and storage. *International Journal of Greenhouse Gas Control* 2010, **4 (5)**: 827-839.

Vilarrasa V, Bolster D, Dentz M, Olivella S, Carrera J. Effects of CO_2 compressibility on CO_2 storage in deep saline aquifers. *Transport In Porous Media* 2010a, **85 (2)**: 619-639.

Vilarrasa V, Bolster D, Olivella S, Carrera J. Coupled hydromechanical modeling of CO_2 sequestration in deep saline aquifers. *International Journal of Greenhouse Gas Control* 2010b, **4 (6)**: 910-919.

Vilarrasa V, Koyama T, Neretnieks I, Jing L. Shear-induced flow channels in a single rock fracture and their effect on solute transport. *Transport In Porous Media* 2011a, **87 (2)**: 503-523.

Vilarrasa V, Olivella S, Carrera J. Geomechanical stability of the caprock during CO_2 sequestration in deep saline aquifers. *Energy Procedia* 2011b, **4**: 5306-5313.

Vilarrasa V, Silva O, Carrera J, Olivella S. Liquid CO_2 injection for geological storage in deep saline aquifers. *International Journal of Greenhouse Gas Control* 2012, *submitted*.

Wileveau Y, Bernier F. Similarities in the hydromechanical response of Callovo-Oxfordian clay and Boom Clay during gallery excavation. *Physics and Chamistry of the Earth* 2008, **33**: 5343-5349.

Xuan R, Sava P. Probabilistic microearthquake location for reservoir monitoring. *Geophysics* 2010, **75 (3)**: MA9-MA26.

Yeo IW, De Freitas MH, Zimmerman RW. Effect of shear displacement on the aperture and permeability of rock. *International Journal of Rock Mechanics and Mining Sciences* 1998, **35(8)**: 1051–1070.

Yin S, Dusseault MB, Rothenburg L. Thermal reservoir modelling in petroleum geomechanics. *International Journal for Numerical and Analytical Methods in Geomechanics* 2009, **33**: 449-485.

Zhang C, Rothfuchs T. Experimental study of the hydro-mechanical behaviour of the Callovo-Oxfordian argillite. *Applied Clay Science* 2004, **26**: 325-336.

Zhang LQ, Yue ZQ, Yang ZF, Qi JX, Liu FC. A displacement-based back-analysis method for rock mass modulus and horizontal in situ stress in tunnelling – Illustrated with a case study. *Tunnelling and Underground Space Technology* 2006, **21**: 636-649.

Zoback MD, Barton CA, Brudy M, Castillo DA, Finkbeiner T, Grollimund BR, Moos DB, Peska P, Ward CD, Wiprut DJ. Determination of stress orientation and magnitude in deep wells. *International Journal of Rock Mechanics and Mining Sciences* 2003, **40**: 1049-1076.

Zoback ML. First and second order patterns of tectonic stress: the world stress map project. *Journal of Geophysical Research* 1992, **97**: 11703-11728.

TABLES

Table 1. Material properties of the aquifer and the caprock

Property	Aquifer	Caprock
Young's modulus, E (GPa)	0.1 – 50	1 - 50
Poisson ratio, ν (-)	0.2 – 0.4	0.2 – 0.4
Friction angle, ϕ' (º)	30	22
Intrinsic permeability, k (m^2)	10^{-13}	10^{-18}
Porosity, ϕ (-)	0.1	0.01

Table 2. Variable definition

Variable	**Definition**
$\Gamma = \frac{G'}{3} + \frac{1}{Le}$	Dimensionless group of the volumetric strain term of the hydromechanical equation. Summation of the pore rigidity ratio and the inverse of the loading efficiency.
$G' = G\phi\beta$	Pore rigidity ratio. Product of rock shear modulus, rock porosity and water compressibility.
$Le = \frac{\alpha}{(\alpha + \phi\beta)}$	Loading efficiency. Ratio of rock compressibility to rock compressibility plus water compressibility multiplied by porosity.
$L = b_{aq}$	The characteristic length has been chosen as the thickness of the aquifer.

$t_D = \frac{\kappa_{aq} t}{L^2 S_s}$	Dimensionless time. Ratio of the product of aquifer hydraulic conductivity and time to the product of the square of the characteristic length and the specific storage coefficient.
$S_s = \rho g(\phi\beta + \alpha)$	Specific storage coefficient. Product of fluid density, gravity and the sum of rock compressibility and water compressibility multiplied by porosity.
$r_D = \frac{r}{L} = \frac{r}{b_{aq}}$	Dimensionless radial distance. Ratio of the radial distance to the characteristic length.
$\Delta P_D = \frac{\Delta P}{h_c \rho g}$	Dimensionless overpressure. Ratio of the overpressure to the product of the characteristic head, fluid density and gravity.
$u_{z_D} = \frac{u_z}{h_c S_s b_{aq}}$	Dimensionless vertical displacement. Ratio of the vertical displacement to the product of characteristic head, specific storage coefficient and aquifer thickness.
$h_c = \frac{Q}{2\pi b_{aq} \kappa_{aq}}$	Characteristic head. Ratio of the flow rate to the product of 2π, aquifer thickness and aquifer hydraulic conductivity.

FIGURE CAPTIONS

Figure 1. Literature review of matrix Young's modulus and Poisson ratio for several sandstones, limestones, dolomitic marble and shales.

Figure 2. Literature review of cohesion and friction angle for several sandstones, limestones, marls, dolomite and shales.

Figure 3. Schematic representation of the hydromechanical characterization test. A sufficiently high water flow rate so as to reach the maximum sustainable injection pressure is injected for several hours. Fluid pressure and displacements or strains are monitored in the aquifer and caprock in as many places as possible (preferably in both the injection and the observation well, but at least in one well).

Figure 4. Mohr-Coulomb failure criterion. Fluid pressure increases due to fluid injection, displacing the Mohr circle to the left. In a favourably oriented cohesionless preexisting fracture, slip occurs when the Mohr circle becomes tangent to the failure envelope (Mohr circle with center *C*'). In intact rock, if the least principal stress equals the rock tensile strength, a hydrofracture will be created perpendicular to its direction (Mohr circle with center *C*''). Alternatively, if deviatoric stress increases and the Mohr circle becomes tangent to the failure envelope, the intact rock will fail along a shear plane. Note that the friction angle of the intact rock may be different from that of a preexisting fracture.

Figure 5. (a) Original (dashed lines) and deformed form of the aquifer and caprock when injecting a fluid in the aquifer. The uplift at the top of the aquifer generates compression in the lower part of the caprock close to the injection well and extension far from it. However, extensions appear in the upper part of the caprock

close to the well and compressions far from it. The mechanical and hydraulic boundary conditions of the problem are also indicated. (b) Volumetric strain and dimensionless fluid pressure change versus dimensionless distance from the injection well at several dimensionless depths. Fluid pressure increases in the contact between the aquifer and the caprock as a result of water injection, leading to an expansion of the aquifer. The pore volume decreases close to the well in the lower part of the caprock because the aquifer uplift compresses it. The pore volume increases close to the well at the top of the caprock due to extension. Fluid pressure in the caprock is inversely proportional to the volumetric strain change. Thus, fluid pressure increases where the pore volume decreases and decreases where the pore volume increases.

Figure 6. (a) Horizontal strain as a function of dimensionless depth at several dimensionless radial distances from the injection well. The injected water displaces the aquifer laterally. The horizontal strain mainly concentrates in the aquifer. Relative displacements between the aquifer and the caprock may occur in the presence of a clay-rich layer with a low friction angle. (b) Vertical strain as a function of dimensionless depth at several dimensionless radial distances from the injection well. The vertical strain is high in the aquifer, where the injected water expands the pore volume, lifting the formation. The caprock, which is pushed upwards, acts as a spring, mitigating the uplift. The grey arrows in the inlets indicate the direction of the strain.

Figure 7. (a) Dimensionless overpressure and (b) dimensionless vertical displacement as a function of the dimensionless group of the volumetric strain term Γ_{aq} at a dimensionless time equal to 1 at the top of the aquifer. Measurements are taken at

an observation well placed at a dimensionless distance of 0.5 from the injection well.

Figure 8. Aquifer Poisson ratio ν_{aq} versus aquifer pore rigidity ratio G'_{aq} for several dimensionless overpressure and dimensionless vertical displacement at the top of the aquifer. Results for a dimensionless time equal to 1 and a dimensionless distance of 0.5 from the injection well. The intersections are possible combinations of the aquifer mechanical properties.

Figure 9. Dimensionless overpressure as a function of the logarithm of dimensionless time at a dimensionless distance of 0.5 from the injection well for several mechanical dimensionless numbers and purely hydraulic simulation (*H*) (a) at the top of the aquifer and (b) at the top of the caprock. As a reference, a dimensionless time equal to 1.0 is achieved in the order of minutes for a stiff rock (big G'_{aq}) and around a day for a soft aquifer (small G'_{aq}).

Figure 10. Dimensionless overpressure at the top of the aquifer as a function of the dimensionless group of the volumetric strain term Γ_{cap} at a dimensionless time equal to 1 at a dimensionless distance of 0.5 from the injection well for several ratios of the caprock to aquifer thickness. The properties of the aquifer are constant. The stiffness and thickness of the caprock alter the aquifer storage coefficient. Stiff thick caprocks lead to a lower aquifer storage coefficient than soft thin caprocks, which advances the pressure buildup response to fluid injection.

Figure 11. Dimensionless vertical displacement at the top of the aquifer and the caprock as a function of the dimensionless group of the volumetric strain term Γ_{cap} at a dimensionless time equal to 1 at a dimensionless distance of 0.5 from the injection

well for several ratios of the caprock to aquifer thickness. The properties of the aquifer are constant. Thick caprocks with low-rigidity can yield subsidence.

Figure 12. Mobilized friction angle at the injection well in the aquifer-caprock contact and at the top of the caprock as a function of the dip angle for soft and stiff aquifers and caprocks for a dimensionless time equal to 1.

Figure 13. Mobilized friction angle at the injection well at the top of the aquifer as a function of time.

Figure 14. Mohr circle representing the stress state of a point. The mobilized friction angle is related to the dip angle of critically oriented fracture, δ, through geometric properties of triangles.

Figure 15. Normal faulting stress regime. (a) Mohr circle at failure, (b) schematic representation of the failure mechanism and (c) plastic deformation obtained from a numerical simulation.

Figure 16. Strike slip faulting stress regime. (a) Mohr circle at failure, (b) schematic representation of the failure mechanism and (c) plastic deformation obtained from a numerical simulation.

Figure 17. Reverse faulting stress regime. (a) Mohr circle at failure, (b) schematic representation of the failure mechanism and (c) plastic deformation obtained from a numerical simulation.

Figure 18. Deviatoric versus mean effective stresses trajectories of a point of the caprock placed 25 m away from the top of the injection well in all directions for a normal, a strike slip and a reverse faulting stress regime.

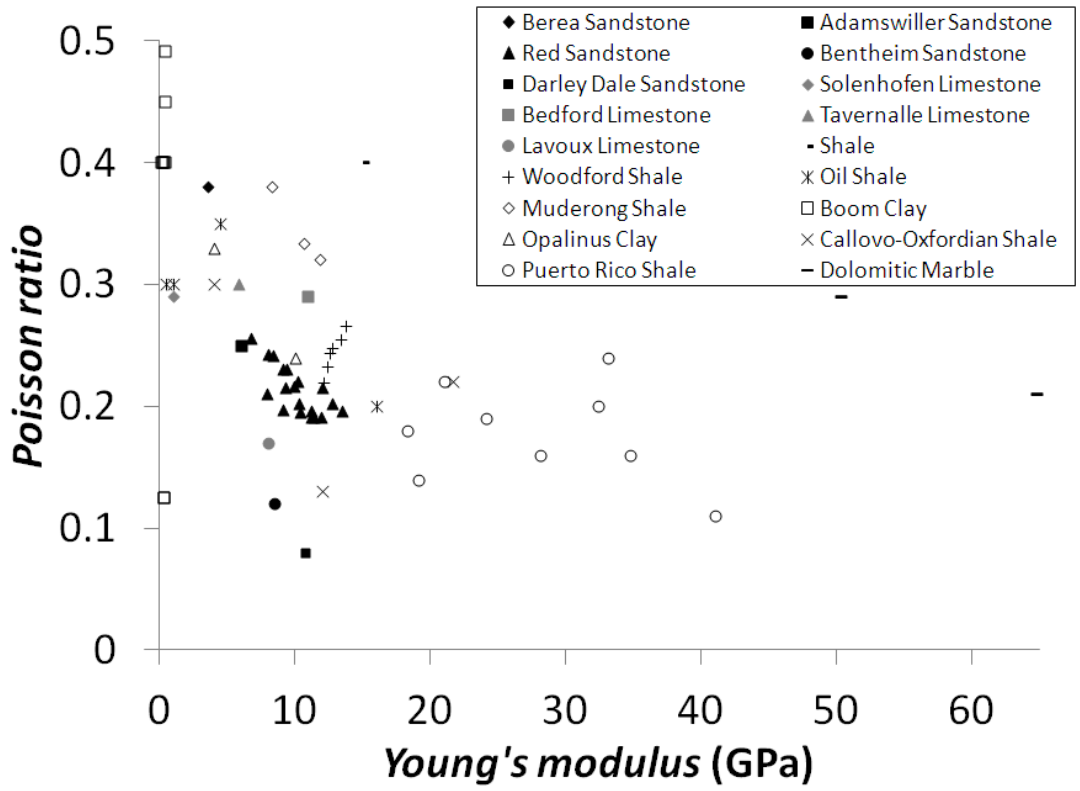
Berea Sandstone
Adamswiller Sandstone
Red Sandstone
Bentheim Sandstone
Darley Dale Sandstone
Solenhofen Limestone
Bedford Limestone
Tavernalle Limestone
Lavoux Limestone
Shale
Woodford Shale
Oil Shale
Muderong Shale
Boom Clay
Opalinus Clay
Callovo-Oxfordian Shale
Puerto Rico Shale
Dolomitic Marble
Poisson ratio
0.5
0.4
0.3
0.2
0.1
0
0
10
20
30
40
50
60
Young's modulus (GPa)

Figure 1

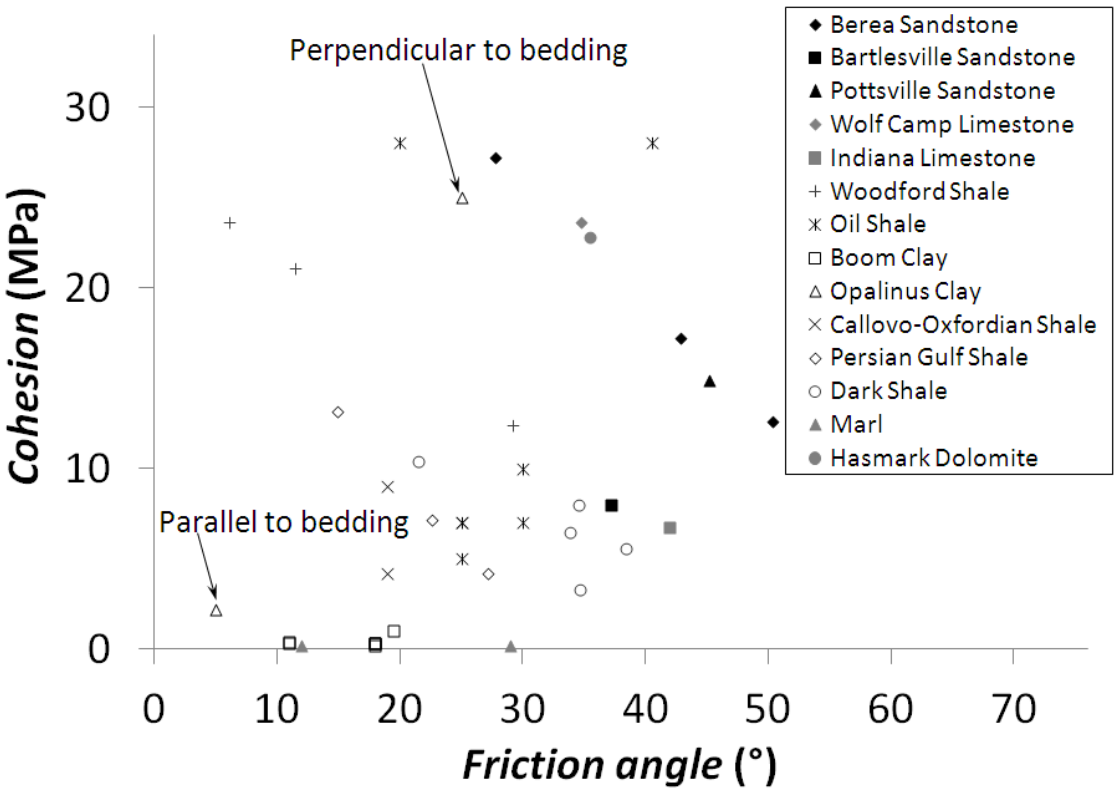
Perpendicular to bedding
Parallel to bedding
Cohesion (MPa)
Friction angle (°)
0
10
20
30
40
50
60
70
Berea Sandstone
Bartlesville Sandstone
Pottsville Sandstone
Wolf Camp Limestone
Indiana Limestone
Woodford Shale
Oil Shale
Boom Clay
Opalinus Clay
Callovo-Oxfordian Shale
Persian Gulf Shale
Dark Shale
Marl
Hasmark Dolomite

Figure 2

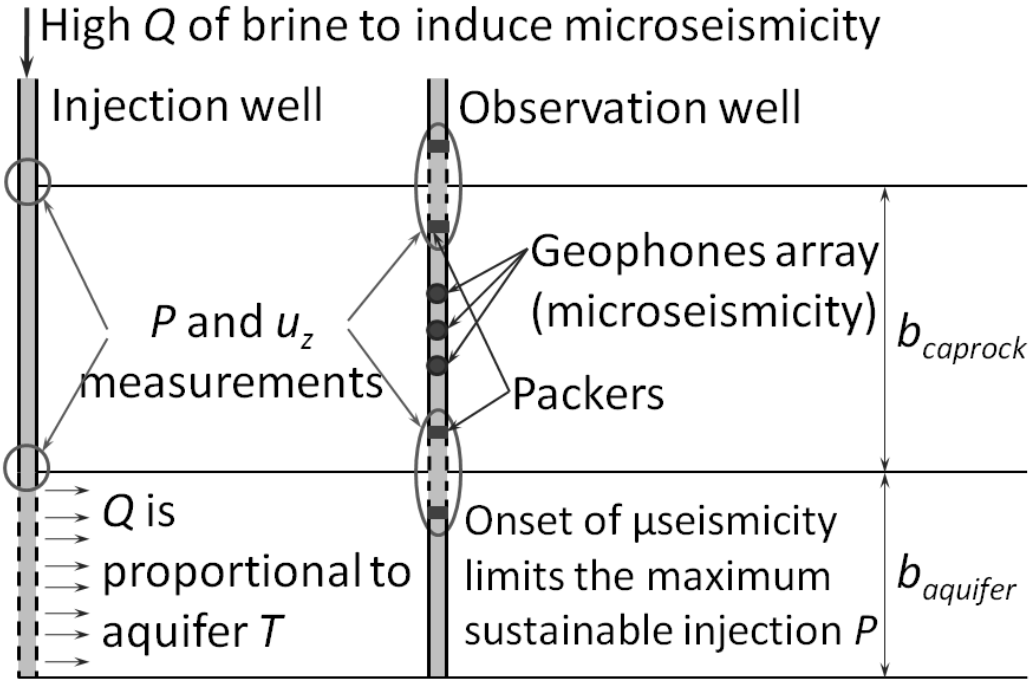
High Q of brine to induce microseismicity
Injection well
Observation well
P and u_z measurements
Geophones array (microseismicity)
Packers
$b_{caprock}$
Q is proportional to aquifer T
Onset of μseismicity limits the maximum sustainable injection P
$b_{aquifer}$

Figure 3

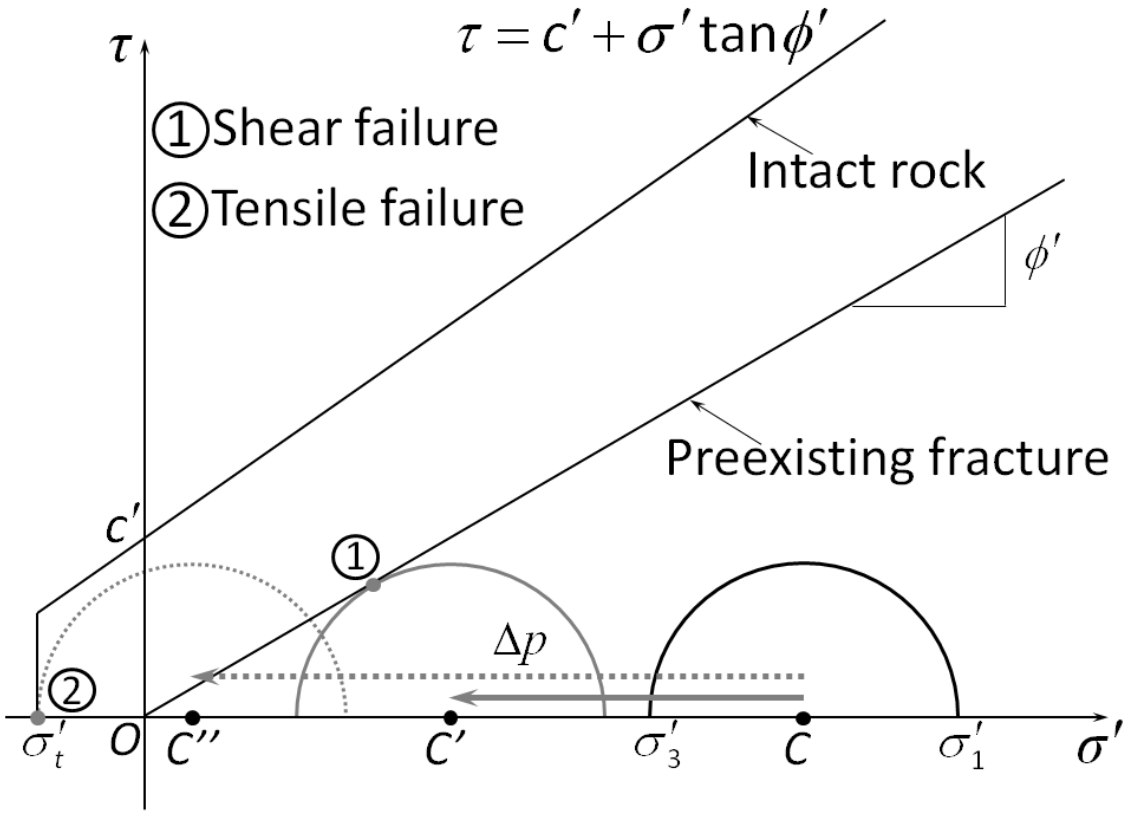
τ
$\tau = c' + \sigma' \tan\phi'$
①Shear failure
②Tensile failure
Intact rock
ϕ'
Preexisting fracture
c'
①
Δp
②
σ_t'
O
C''
C'
σ_3'
C
σ_1'
σ'

Figure 4

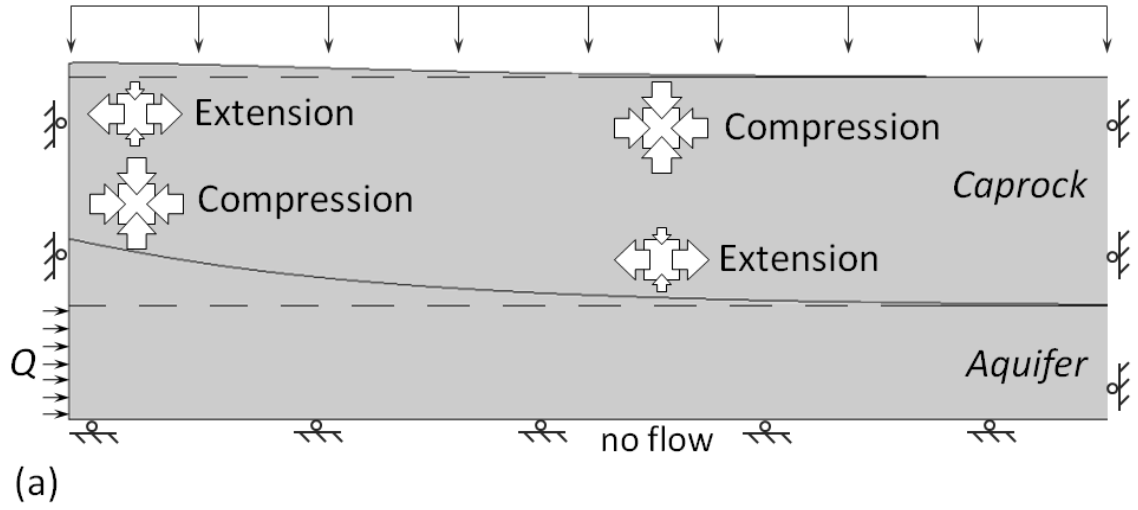

Figure 5a

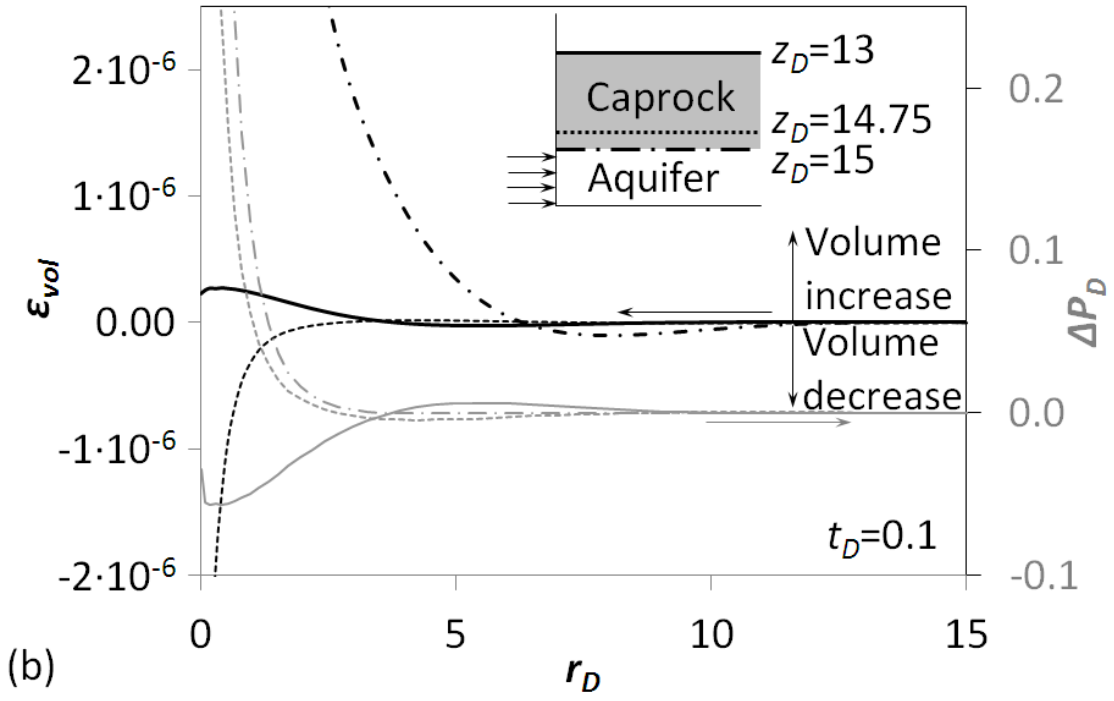

Figure 5b

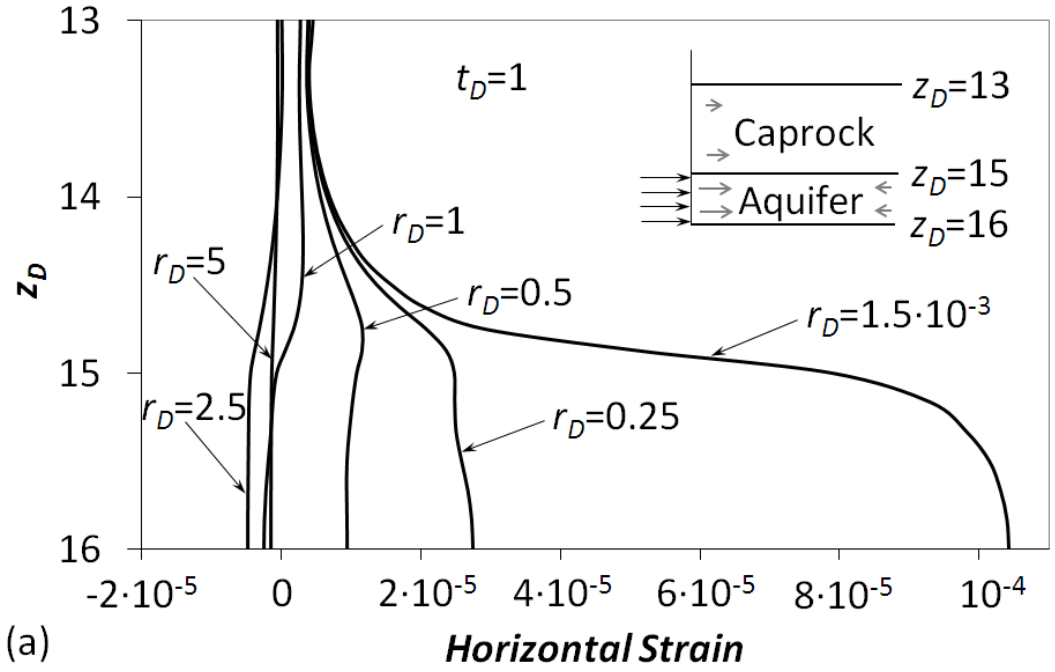

Figure 6a

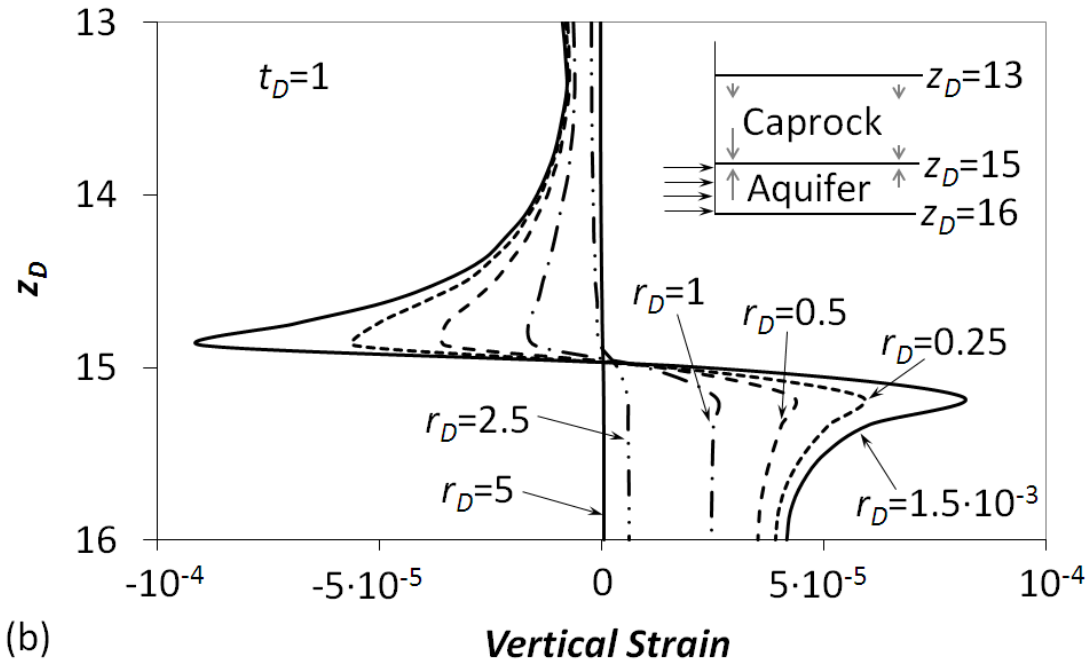

Figure 6b

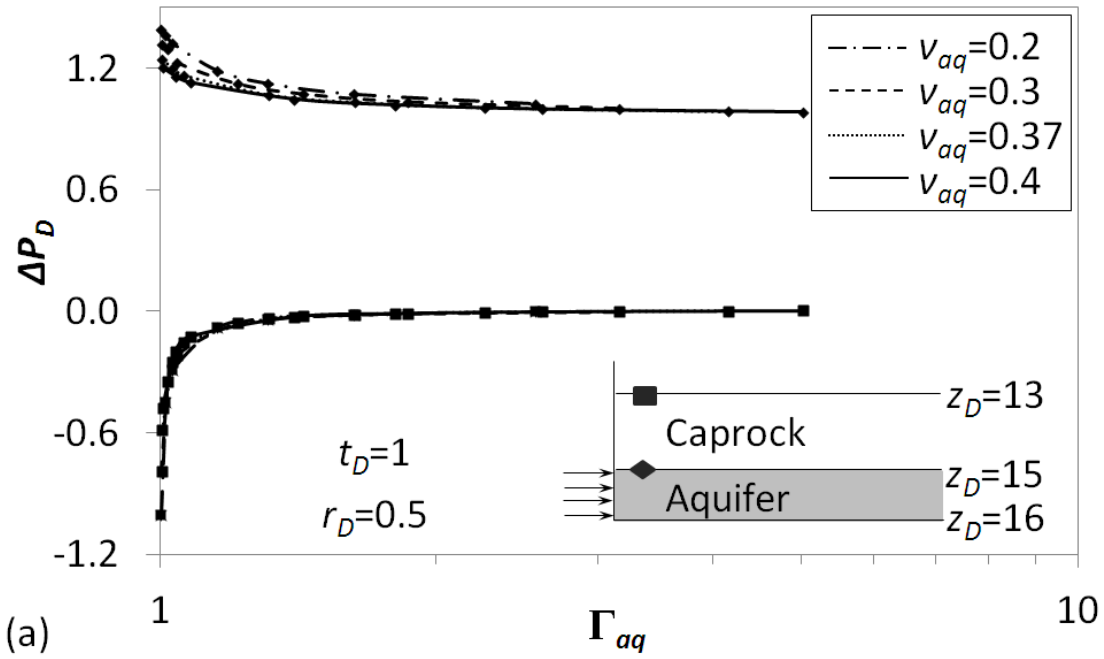

Figure 7a

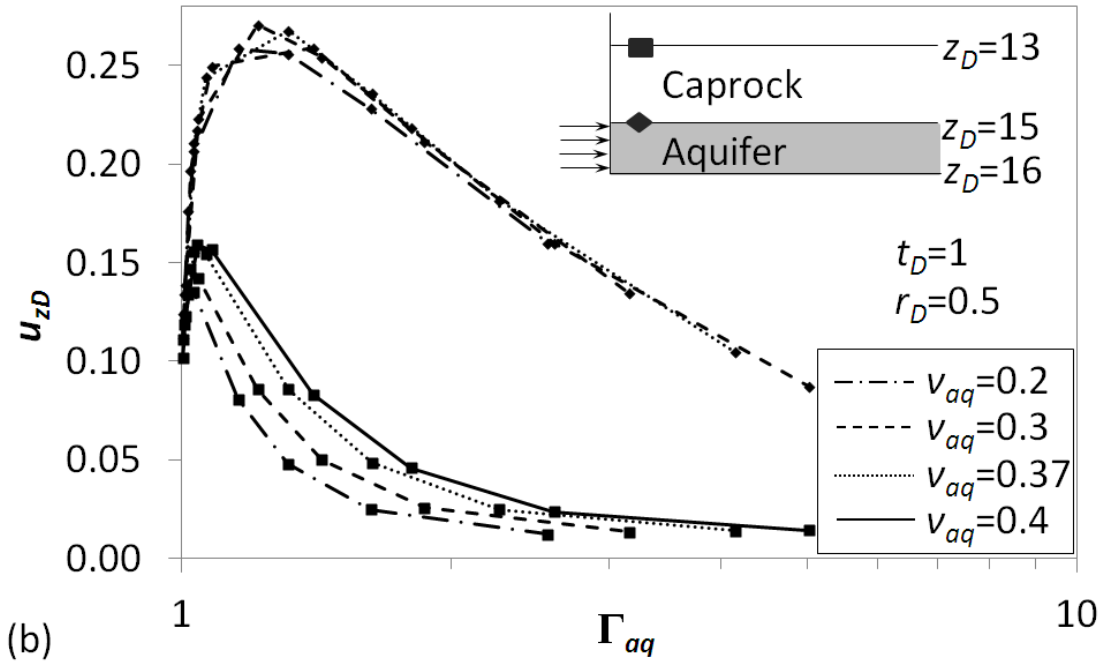

Figure 7b

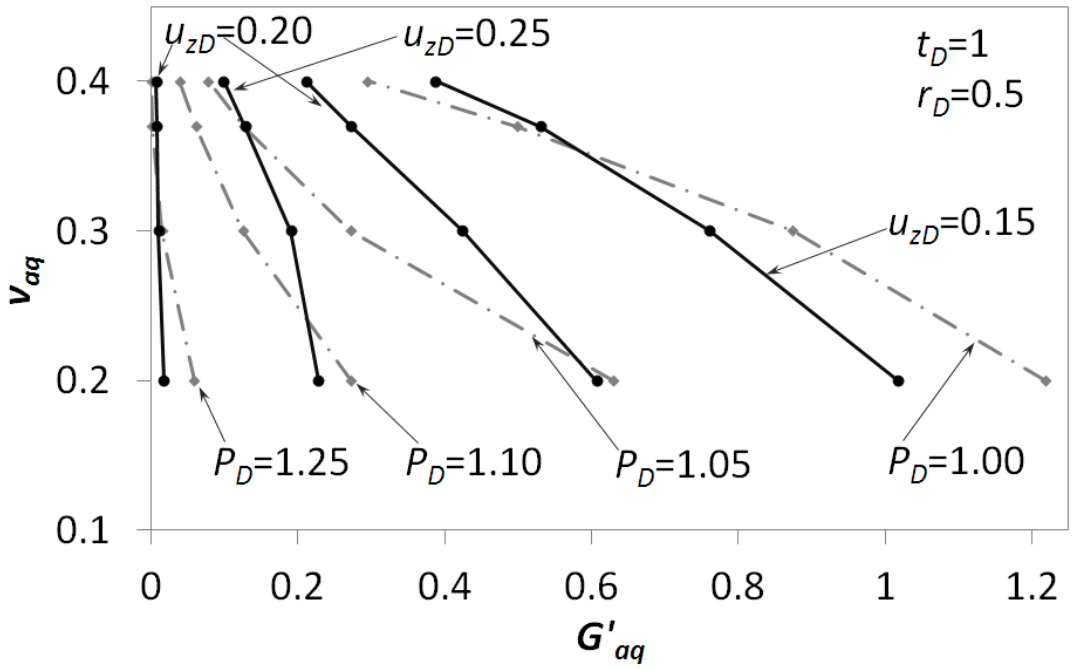
u_{zD}=0.20
u_{zD}=0.25
t_D=1
r_D=0.5
u_{zD}=0.15
P_D=1.25
P_D=1.10
P_D=1.05
P_D=1.00
v_{aq}
G'_{aq}
0.4
0.3
0.2
0.1
0
0.2
0.4
0.6
0.8
1
1.2

Figure 8

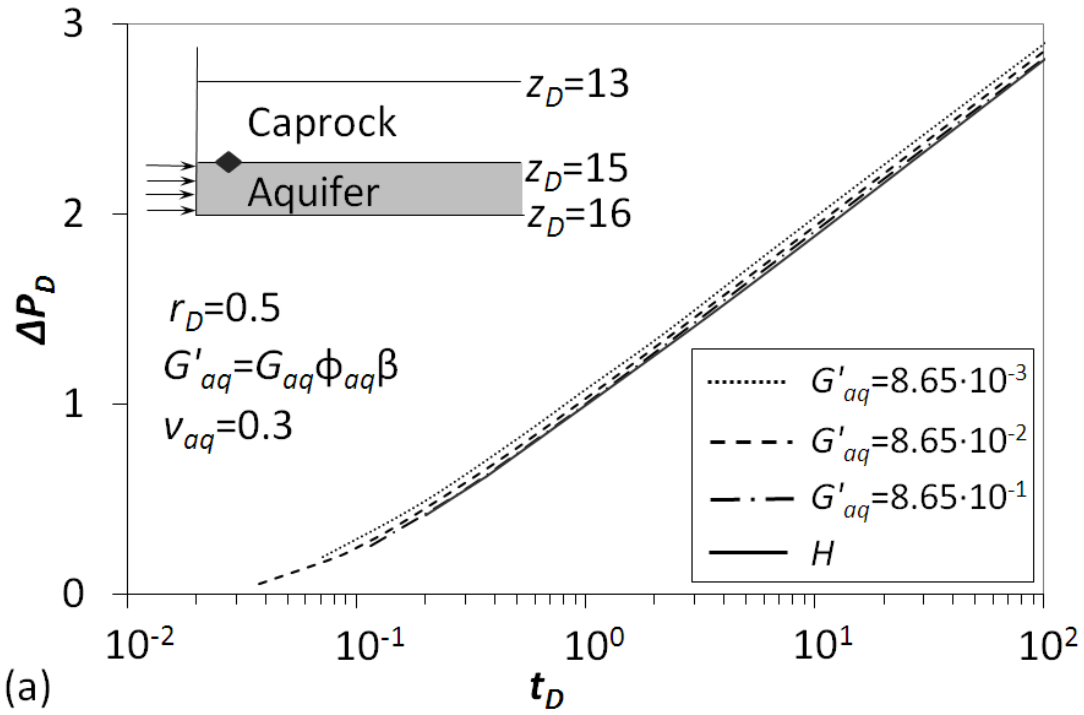

Figure 9a

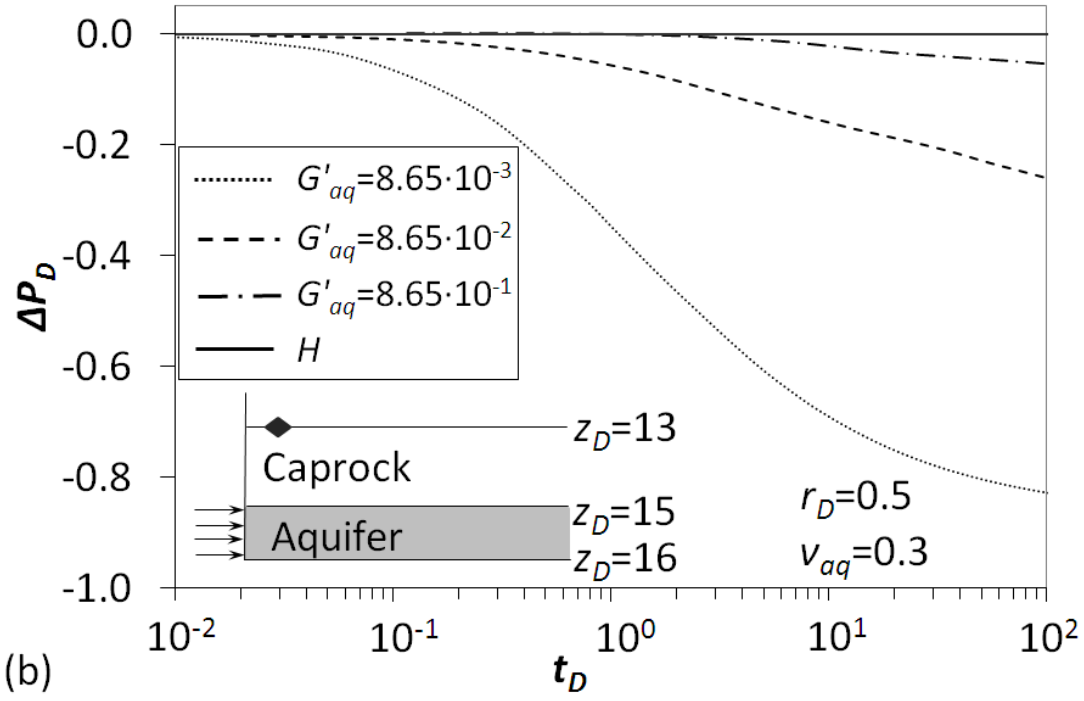

Figure 9b

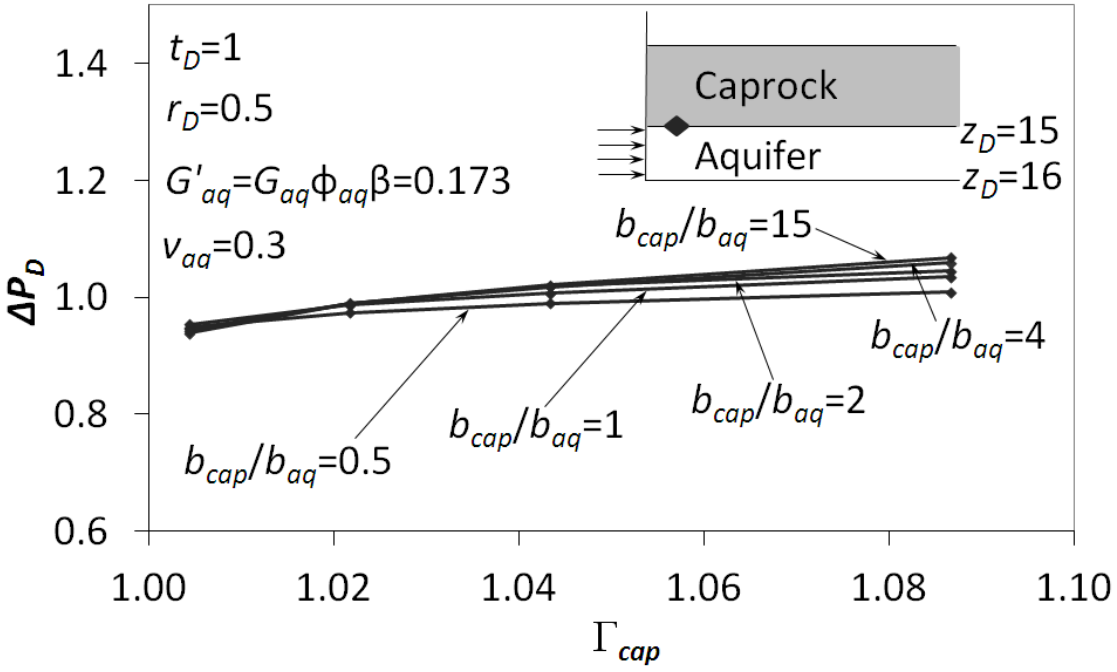
t_D=1
r_D=0.5
$G'_{aq}=G_{aq}\phi_{aq}\beta$=0.173
v_{aq}=0.3
Caprock
Aquifer
z_D=15
z_D=16
b_{cap}/b_{aq}=15
b_{cap}/b_{aq}=4
b_{cap}/b_{aq}=2
b_{cap}/b_{aq}=1
b_{cap}/b_{aq}=0.5
ΔP_D
Γ_{cap}
1.4
1.2
1.0
0.8
0.6
1.00
1.02
1.04
1.06
1.08
1.10

Figure 10

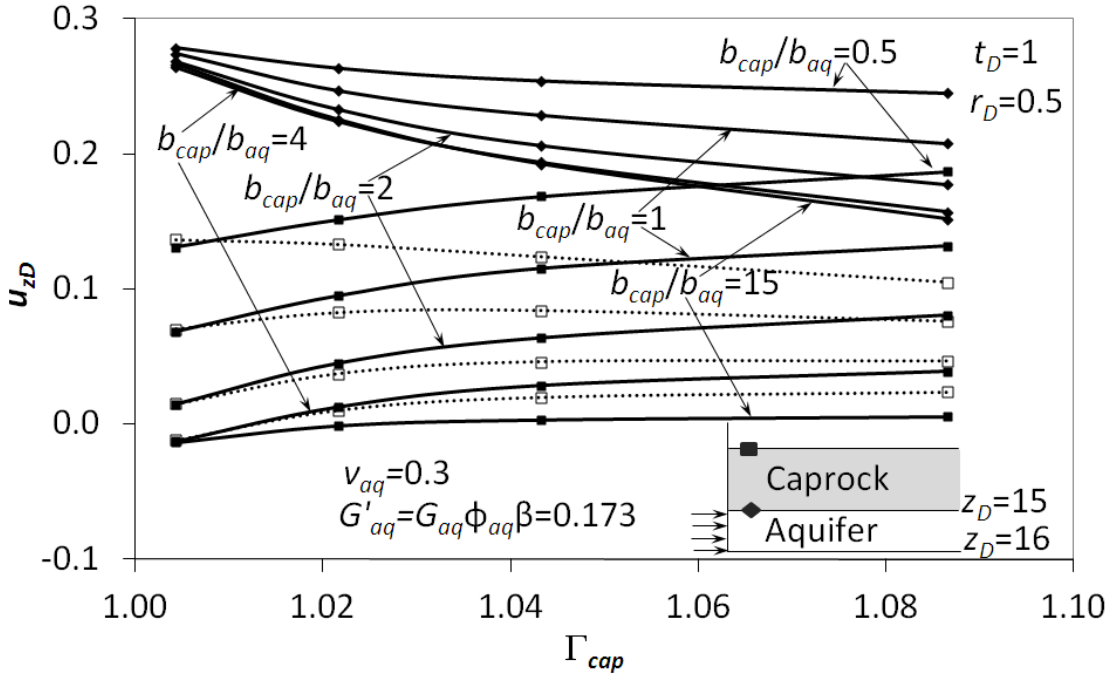
0.3
0.2
0.1
0.0
-0.1
u_{zD}
1.00
1.02
1.04
1.06
1.08
1.10
Γ_{cap}
b_{cap}/b_{aq}=0.5
t_D=1
r_D=0.5
b_{cap}/b_{aq}=4
b_{cap}/b_{aq}=2
b_{cap}/b_{aq}=1
b_{cap}/b_{aq}=15
v_{aq}=0.3
$G'_{aq}=G_{aq}\phi_{aq}\beta$=0.173
Caprock
Aquifer
z_D=15
z_D=16

Figure 11

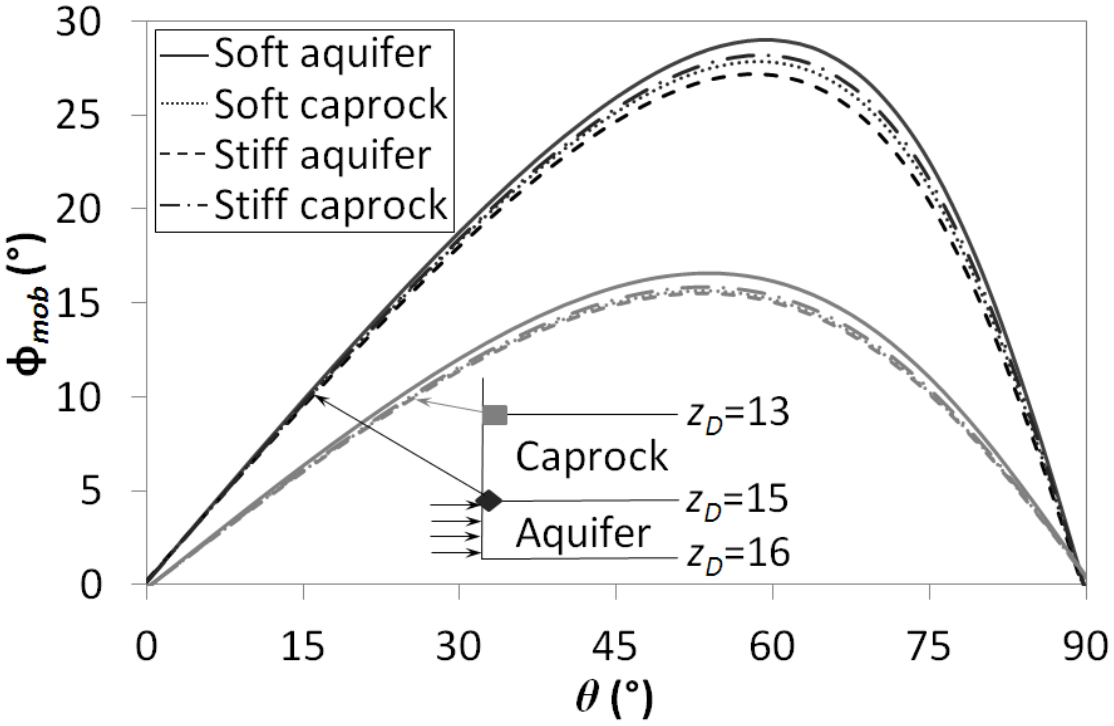
Soft aquifer
Soft caprock
Stiff aquifer
Stiff caprock
ϕ_{mob} (°)
θ (°)
0
5
10
15
20
25
30
0
15
30
45
60
75
90
z_D=13
Caprock
z_D=15
Aquifer
z_D=16

Figure 12

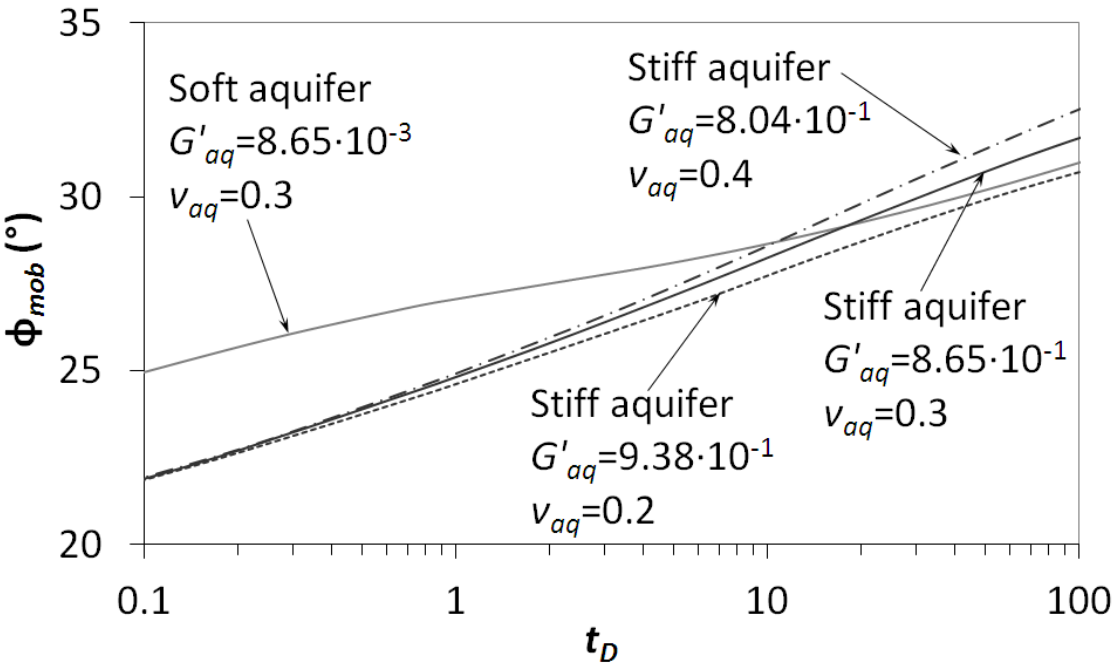
35
30
25
20
0.1
1
10
100
Φ_{mob} (°)
t_D
Soft aquifer
G'_{aq}=8.65·10^{-3}
v_{aq}=0.3
Stiff aquifer
G'_{aq}=8.04·10^{-1}
v_{aq}=0.4
Stiff aquifer
G'_{aq}=9.38·10^{-1}
v_{aq}=0.2
Stiff aquifer
G'_{aq}=8.65·10^{-1}
v_{aq}=0.3

Figure 13

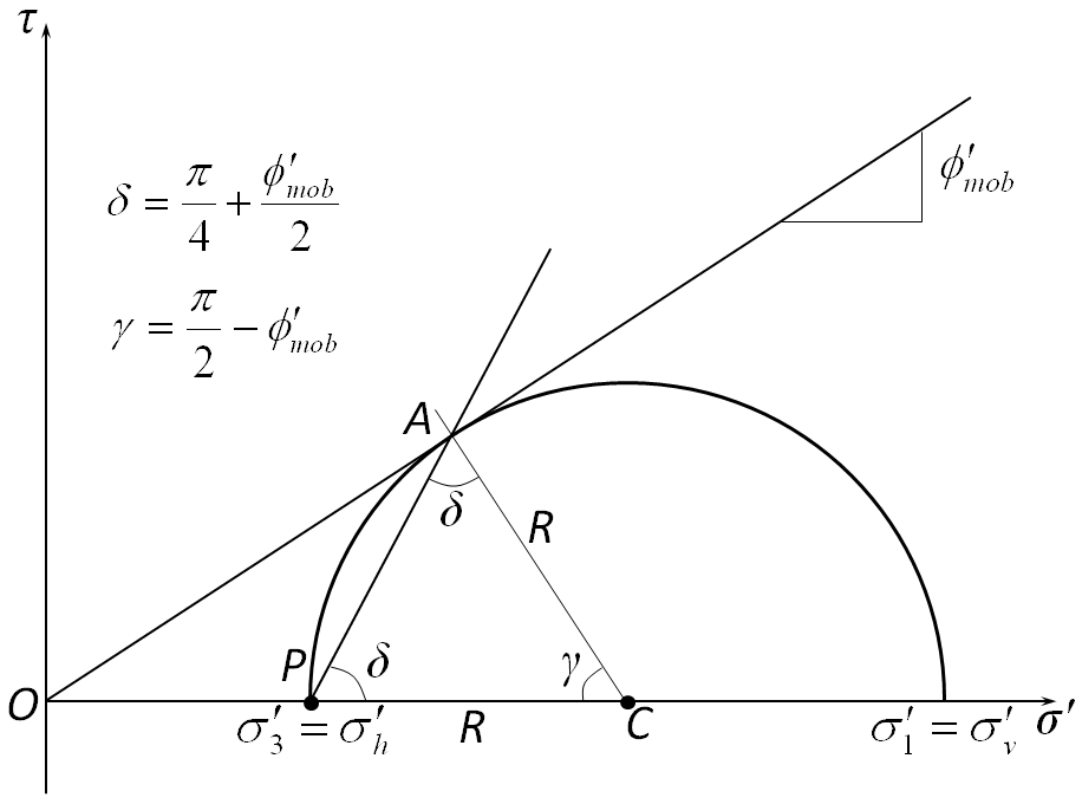
τ
$\delta = \frac{\pi}{4} + \frac{\phi'_{mob}}{2}$
$\gamma = \frac{\pi}{2} - \phi'_{mob}$
ϕ'_{mob}
A
δ
R
P
δ
γ
O
$\sigma'_3 = \sigma'_h$
R
C
$\sigma'_1 = \sigma'_v$
σ′

Figure 14

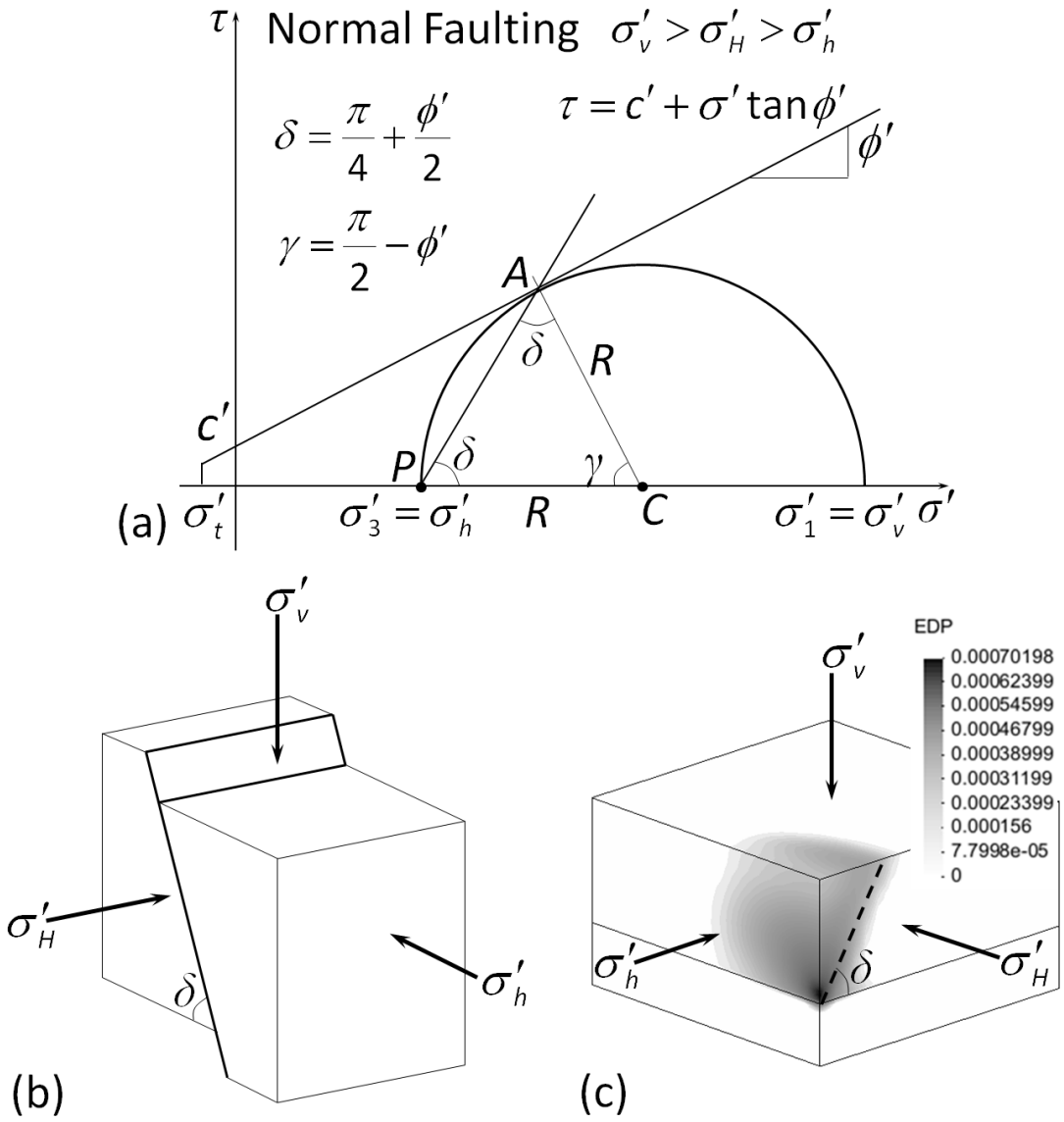
τ
Normal Faulting $\sigma'_v > \sigma'_H > \sigma'_h$
$\delta = \frac{\pi}{4} + \frac{\phi'}{2}$
$\tau = c' + \sigma' \tan\phi'$
ϕ'
$\gamma = \frac{\pi}{2} - \phi'$
A
δ
R
c'
P
δ
γ
(a)
σ'_t
$\sigma'_3 = \sigma'_h$
R
C
$\sigma'_1 = \sigma'_v$ σ'
σ'_v
σ'_H
δ
σ'_h
(b)
EDP
0.00070198
0.00062399
0.00054599
0.00046799
0.00038999
0.00031199
0.00023399
0.000156
7.7998e-05
0
σ'_v
σ'_h
δ
σ'_H
(c)

Figure 15

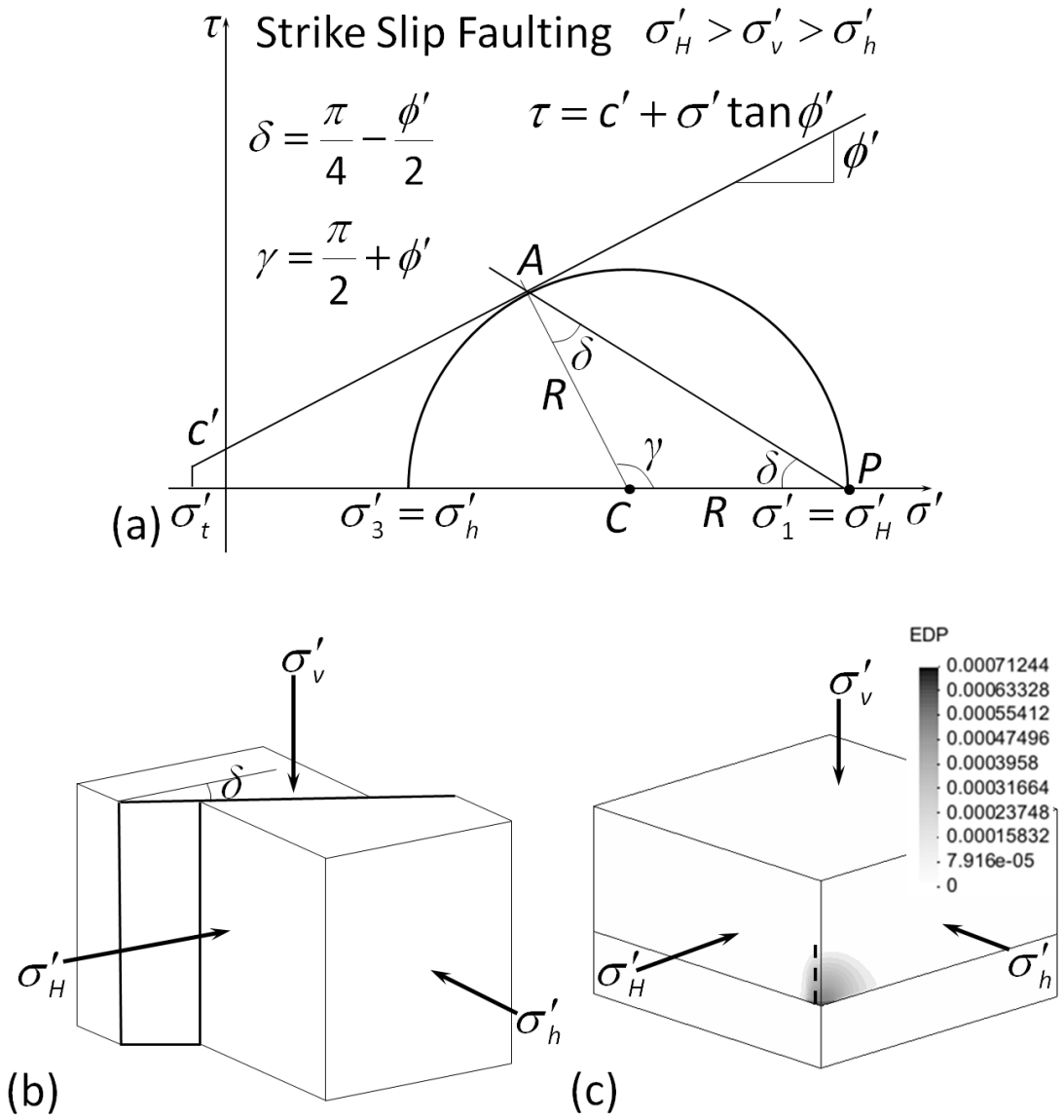
τ
Strike Slip Faulting $\sigma'_H > \sigma'_v > \sigma'_h$
$\delta = \frac{\pi}{4} - \frac{\phi'}{2}$
$\tau = c' + \sigma' \tan\phi'$
ϕ'
$\gamma = \frac{\pi}{2} + \phi'$
A
δ
R
c'
γ
δ
P
(a)
σ'_t
$\sigma'_3 = \sigma'_h$
C
R
$\sigma'_1 = \sigma'_H$
σ'
σ'_v
δ
σ'_H
σ'_h
(b)
EDP
0.00071244
0.00063328
0.00055412
0.00047496
0.0003958
0.00031664
0.00023748
0.00015832
7.916e-05
0
σ'_v
σ'_H
σ'_h
(c)

Figure 16

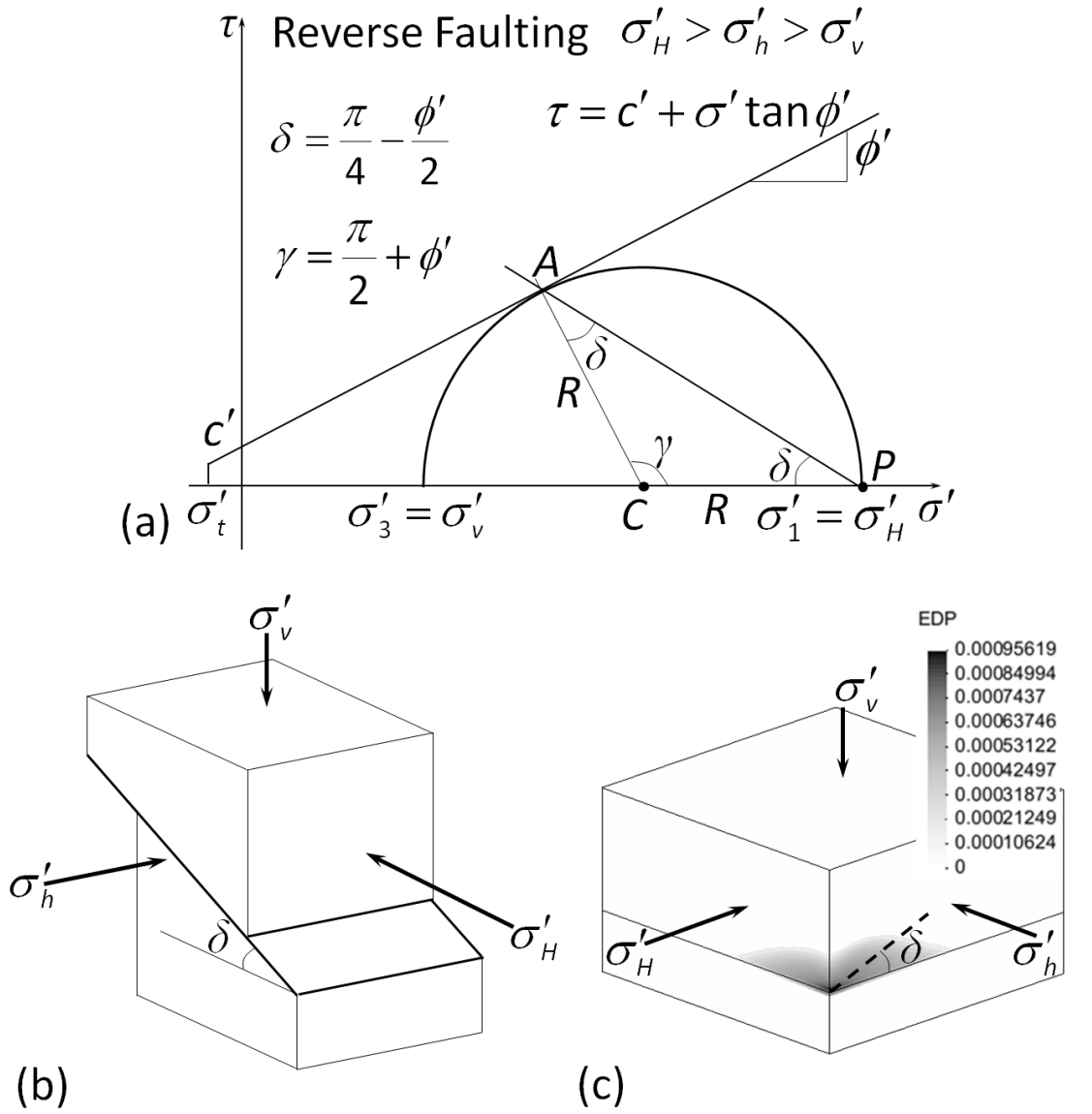
τ
Reverse Faulting $\sigma'_H > \sigma'_h > \sigma'_v$
$\delta = \frac{\pi}{4} - \frac{\phi'}{2}$
$\tau = c' + \sigma' \tan\phi'$
ϕ'
$\gamma = \frac{\pi}{2} + \phi'$
A
δ
R
c'
γ
δ
P
(a)
σ'_t
$\sigma'_3 = \sigma'_v$
C
R
$\sigma'_1 = \sigma'_H$
σ'
σ'_v
σ'_h
δ
σ'_H
(b)
EDP
0.00095619
0.00084994
0.0007437
0.00063746
0.00053122
0.00042497
0.00031873
0.00021249
0.00010624
0
σ'_v
σ'_H
δ
σ'_h
(c)

Figure 17

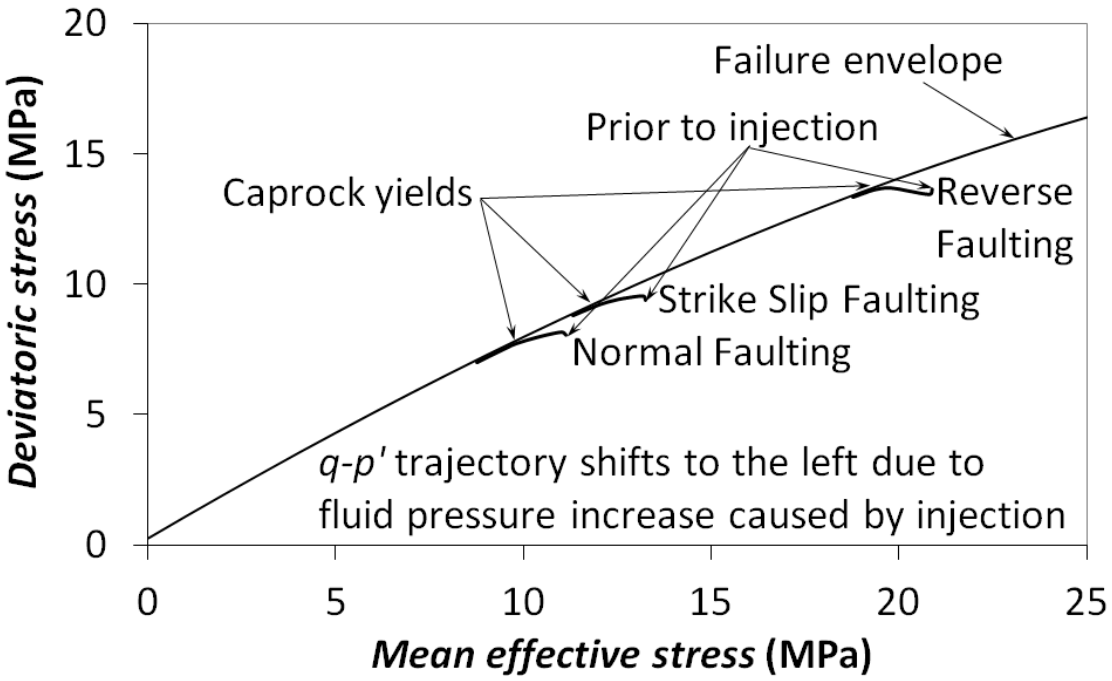
Failure envelope
Prior to injection
Caprock yields
Reverse
Faulting
Strike Slip Faulting
Normal Faulting
q-p' trajectory shifts to the left due to
fluid pressure increase caused by injection
Deviatoric stress (MPa)
Mean effective stress (MPa)
0
5
10
15
20
25

Figure 18